CALCULATING AND LIMITING LOCAL STRAINS IN GEOMEMBRANES FROM GRAVEL INDENTATIONS

by

Michael Keith Eastman

A thesis submitted to the Department of Civil Engineering

In conformity with the requirements for

the degree of Master of Applied Science

Queen's University

Kingston, Ontario, Canada

(September, 2013)

Dedication

This thesis is dedicated to my father who I look up to in so many ways and my mother who has always believed in me.

Abstract

Short-term tensile strains that arise from local gravel indentations in municipal solid waste landfill base geomembrane liners are investigated with an emphasis on quantifying how strains are obtained and providing methods for limiting long-term local geomembrane strains below allowable levels. This involved the development of new experimental techniques and apparatuses to study geomembrane strains under controlled conditions.

An experimental technique to measure the radial and vertical components of displacement from local gravel indentations in a geomembrane is presented. Geomembrane strains were calculated using large strain-displacement theory, thin shell theory, and the arc elongation method. While radial displacements were found to be small relative to vertical displacements, they were shown to provide the dominant contribution to the maximum strain beneath the centre of the gravel indentation. Both the thin shell and arc elongation methods produced incorrect distributions of strain and also provided magnitudes that significantly underestimated the maximum geomembrane strain.

Small-scale screening tests were conducted to gain insight into how key factors including the compressibility of the underlying clay layer, particle size of the overlying gravel, and mass of the geotextile protection layer influence local geomembrane strains. Results are provided that can be used to rule out protection layers that are unable to meet a long-term strain limit, and conversely, identify those that may be able to limit strains below a target strain for further larger scale evaluation. Compaction water contents towards the lower range of water content to achieve an acceptably low hydraulic conductivity of field compacted clay liners were found to be more successful in limiting local strains in the geomembrane. Protection from geotextiles with masses up to 2440 g/m^2 were unable to limit geomembrane strains below 1.5% with nominal 50 mm gravel at a temperature of 55°C. Tests with nominal 25 mm gravel revealed that a geotextile with a mass of 1500 g/m^2 successfully limited the maximum geomembrane

strain below 1.5% at an applied stress of 250 kPa while another geotextile (2440 g/m^2) met the strain limit up to applied stresses of 500 kPa at a temperature of 55°C.

Co-Authorship

This thesis contains materials submitted for publication that have been co-authored by M. Eastman and his supervisor, Dr. R.W.I Brachman. The research reported in this thesis was initiated by consultation between M. Eastman and Dr. R.W.I. Brachman. The laboratory tests were planned and conducted by M. Eastman. The analysis and interpretation of laboratory data was performed by M. Eastman under the direct supervision of Dr. R.W.I. Brachman.

Acknowledgements

The wisdom, support, and enthusiasm from my supervisor, Dr. R.W.I. Brachman has been invaluable in completing this thesis. I am extremely grateful for his patience and encouragement throughout the entire research duration.

Funding was made possible by the generous support from the Natural Sciences and Engineering Research Council of Canada (NSERC) and by the Canadian Foundation for Innovation (CFI).

Thank you to Dr. Ali Sabir and Dr. Simon Gudina for sharing their knowledge and assisting me in the initial stages of my research. Their insight and guidance was tremendously helpful.

The support and technical staff were overwhelmingly helpful and friendly. Thank you to Mr. Cory Mitchell, Ms. Diann King, Mr. Jaime Escobar, Ms. Maxine Wilson, Mr. Neil Porter, Mr. Paul Thrasher, and Mr. Stan Prunster for their exceptional assistance and support.

Thank you to my friends and colleagues in the Civil Engineering Department for creating such a positive environment. I thank Mr. Fady Abdelaal, Mr. Jean-Marc LeBlanc, Mr. Mohamed Hosney, and Mr. Prabeen Joshi for assisting me in the laboratory whenever help was needed.

Finally, I thank my friends and family for constantly believing in me.

Table of Contents

List of Figures

CHAPTER 2

CHAPTER 3

List of Tables

CHAPTER 2

CHAPTER 3

Chapter 1

Introduction

1.1 Description of problem

Modern engineered landfills typically incorporate a barrier system consisting of a composite liner and an overlying leachate collection system to minimize the transport of contaminants into the environment and to ensure that any migration of contaminants is below allowable levels (e.g., see Rowe et al., 2004). Geomembranes are commonly used with a low permeable layer such as compacted clay or a geosynthetic clay liner to form the composite liner. The material of choice for landfill geomembranes is typically high-density polyethylene with a thickness generally ranging between 1.5-2.5 mm.

Geomembranes significantly enhance barrier system performance since they are essentially impermeable, as long as the liner is free of holes or flaws. However, the use of coarse gravel in the overlying leachate collection system can result in the formation of holes in a geomembrane and therefore poses a puncture risk to the integrity of a barrier system. A protection layer is therefore required when incorporating geomembranes in landfill barrier systems to prevent geomembrane puncture (e.g., Koerner et al., 2010). When large overburden pressures act on the barrier system, coarse gravel in the leachate collection system can produce indentations in the geomembrane. Consequently, these gravel induced indentations result in geomembrane strains which may cause long-term local brittle rupture of the geomembrane. If the geomembrane were to be ruptured, the integrity of the barrier system would be compromised, potentially leading to the transport of contaminants into the environment.

1.2 Current state of practice

A common approach to obtain strains in a geomembrane is to calculate the resulting strains based on the deformed shape of a geomembrane (Saathoff and Sehrbrock, 1994; Dixon et al. 1997; Gallager et al. 1999; Zanzinger, 1999; Tognon et al. 2000; Gudina and Brachman, 2006; Hornsey and Wishaw, 2012). Deformations of the geomembrane are normally obtained by measuring the permanent indentation on a soft lead sheet placed beneath the geomembrane. Subsequent geomembrane strains are typically calculated using thin shell theory developed by Tognon et al. (2000). The most significant assumption with thin shell theory is that there are only vertical displacements and no radial displacements of the geomembrane. The potential influence of radial displacements when calculating geomembrane strain from gravel indentations is not known.

To prevent geomembrane puncture from overlying coarse gravel in the leachate collection system, a nonwoven needle-punched geotextile is commonly placed on top of the geomembrane to serve as a protection layer. The design approach developed by Narejo et al. (1996) and then updated by Koerner et al. (2010) is often followed to select a protection geotextile. Depending on the size of the overlying gravel and overburden stress, a mass for the geotextile is selected. In previous studies (Tognon et al., 2000; Gudina and Brachman, 2006; Dickinson and Brachman, 2008; Brachman and Gudina, 2008) tests were conducted with nominal 50 mm gravel overlying a 1.5-mm-thick high-density polyethylene geomembrane on top of a compacted clay liner and/or a geosynthetic clay liner. Geotextile protection that met design criteria outlined in Narejo et al. (1996) was used. While no puncture was observed in the geomembrane for test times varying between 10 and 100 h at 250 kPa of applied stress, geomembrane strains exceeded the long-term allowable strain limit of 3% proposed by Seeger and Müller (2003). While it is well understood that geomembrane protection can reduce strains that develop in a geomembrane, other factors may also limit geomembrane strains including a

firmer foundation layer, smaller gravel size, or thicker geomembrane. Thus, there exists a need to investigate other factors that can potentially limit local geomembrane strains below long-term allowable limits.

1.3 Research objectives and methodology

This thesis examines the deformations and strains that occur in a high-density polyethylene geomembrane typically used as part of a composite liner at the base of modern engineered landfills, the main emphasis being placed on a 1.5-mm-thick high-density polyethylene geomembrane. The specific objectives of this research are to:

- present an experimental technique to measure radial and vertical displacements of a high-density polyethylene geomembrane and compare the local strains calculated using large strain-displacement theory with thin shell and arc elongation methods; and
- provide insight into how key factors including the compressibility of the underlying clay, particle size of the overlying gravel, and type of protection layer impact local geomembrane strains through screening tests which can then be used to rule out protection layers that are unable to meet a long-term tensile strain limit.

These objectives were achieved by planning and conducting a series of laboratory tests designed to measure and quantify the parameters being studied. Tests performed in Chapter 2 were conducted in a test apparatus previously developed by Sabir and Brachman (2012) to simulate the mean local strains induced by nominal 50 mm gravel. Tests performed in Chapter 3 were conducted with two new test apparatuses designed to simulate the mean local strains induced by nominal 50 and 25 mm gravel.

1.4 Scope of the thesis

The original contributions described in this thesis are summarized in the following sections.

1.4.1 Chapter 2 – Calculating local geomembrane indentation strains from measured radial and vertical displacements

An experimental technique was developed to measure the radial and vertical components of displacement in a 1.5-mm-thick high-density polyethylene geomembrane from a nominal 50 mm gravel particle. The influence of radial displacements when calculating the maximum strain was examined. Geomembrane strains were calculated using large strain-displacement theory, thin shell theory, and the arc elongation method.

1.4.2 Chapter 3 – Screening tests to help limit local geomembrane strains from gravel indentations

Two test apparatuses were deigned to simulate the mean local strains induced by nominal 50 and 25 mm gravel. Small-scale screening tests were conducted to provide insight into how compressibility of the underlying clay, particle size of the overlying gravel, and type of protection layer impact local geomembrane strains. These results could be used to screen out protection layers that do not meet long-term strain limits while identifying those that may be able to limit strains to a target level for subsequent larger scale evaluation.

1.5 Format of the thesis

This thesis has been prepared in accordance with the regulations for a Manuscript Form thesis as stipulated by the School of Graduate Studies at Queen's University. Each manuscript is presented with the literature review, experimental methodology, results, and conclusions

pertinent to each contribution, but without an abstract. References, tables, and figures are presented at the end of each chapter. The thesis consists of two original manuscripts in Chapters 2-3. Chapter 2 has been accepted for publication. Chapter 3 will be submitted for publication. Additional information is included in the appendices. Units of measurement corresponding to the S.I. system (*Le Système International d'Unités*) are used consistently throughout the thesis.

1.6 References

Brachman, R.W.I., Gudina, S., 2008. Geomembrane strains from coarse gravel and wrinkles in a GM/GCL composite liner. Geotextiles and Geomembranes 26 (6), 488-497.

Dickinson, S., Brachman, R.W.I., 2008. Assessment of alternative protection layers for a geomembrane / geosynthetic clay liner (GM/GCL) composite liner. Canadian Geotechnical Journal 45 (11), 1594-1610.

Dixon, N., Jones, D.R.V., Hayden, J., 1997. Performance of geoprotectors for landfill liners. Proc., Geoenvironmental Engineering Conference, Cardiff, UK, 351-356.

Gallagher, E.M., Darbyshire, W., Warwick, R.G., 1999. Performance testing of landfill geoprotectors: Background, critique, development and current practice. Geosynthetics International 6 (4), 283-301.

Gudina, S., Brachman, R.W.I., 2006. Physical response of geomembrane wrinkles overlying compacted clay. Journal of Geotechnical and Geoenvironmental Engineering 132 (10), 1346-1353.

Hornsey, W.P., Wishaw, D.M., 2012. Development of a methodology for the evaluation of geomembrane strain and relative performance of cushion geotextiles. Geotextiles and Geomembranes 35, 87-99.

Koerner, R.M., Hsuan, Y.G., Koerner, G.R., Gryger, D., 2010. Ten year creep puncture study of HDPE geomembranes protected by needle-punched nonwoven geotextiles. Geotextiles and Geomembranes 28 (6), 503-513.

Narejo, D., Koerner, R.M., Wilson-Fahmy, R.F., 1996. Puncture protection of geomembranes, part II: experimental. Geosynthetics International, 3 (5), 629-653.

Rowe, R.K., Quigley, R.M., Brachman, R.W.I., and Booker, J.R., 2004. Barrier Systems for Waste Disposal Facilities. 2nd Ed., E & FN Spon, London, 587 pp.

Saathoff, F., Sehrbrock, U., 1994. Indicators for selection of protection layers for geomembranes. Proc., Fifth International Conference on Geotextiles, Geomembranes and Related Products, Singapore, 1019-1022.

Sabir, A., Brachman, R.W.I., 2012. Time and temperature effects on geomembrane strain from a gravel particle subject to sustained vertical force. Canadian Geotechnical Journal, 49 (3), 249-263.

Seeger, S., Müller, W., 2003. Theoretical approach to designing protection: selecting a geomembrane strain criterion. Geosynthetics: Protecting the Environment. Dixon, N., Smith, D.M., Greenwood, J.H., Jones, D.R.V. (Eds.), Thomas Telford, London, 137-152.

Tognon, A.R., Rowe, R.K., Moore, I.D., 2000. Geomembrane strain observed in large-scale testing of protection layers. ASCE Journal of Geotechnical and Geoenvironmental Engineering 126 (12), 1194-1208.

Zanzinger, H., 1999. Efficiency of geosynthetic protection layers for geomembrane liners: performance in a large-scale model test. Geosynthetics International 6 (4), 303-317.

Chapter 2

Calculating local geomembrane indentation strains from measured radial and vertical displacements[1]

2.1 Introduction

Protection layers are required above landfill geomembranes to limit short-term puncture during construction and to reduce the potential for long-term rupture at local indentations from overlying coarse gravel particles when subject to overburden stresses, Fig. 2.1 (e.g., Rowe et al., 2004; Koerner et al., 2010). Development of any holes from short-term puncture or long-term rupture would increase the leakage though the geomembrane and hence reduce its effectiveness as an environmental liner (e.g., Rowe 2012). Assessment of the long-term effectiveness of the protection layer should involve limiting the local tensile strains induced in the geomembrane below allowable limits. For example, long-term allowable tensile strain limits ranging between 3-8% have been proposed (Seeger and Müller, 2003; Peggs et al., 2005) with the intent of reducing the potential for long-term brittle rupture of the geomembrane. Physical experiments are typically conducted to assess the depth of the local indentations in the geomembrane and the resulting magnitude of local tensile strains (e.g., Saathoff and Sehrbrock, 1994; Dixon et al., 1997; Gallager et al., 1999; Zanzinger, 1999; Tognon et al., 2000; Gudina and Brachman, 2006; Hornsey and Wishaw, 2012). This paper focusses on how strains are obtained from local indentations in the geomembrane.

Conceivably, two approaches can be used to obtain local geomembrane strains. The first approach involves the use of electrical foil strain gauges. However, two significant issues

[1]This chapter has been previously published as: Brachman, R.W.I., Eastman, M.K., 2013. Calculating local geomembrane indentation strains from measured radial and vertical displacements. Geotextiles and Geomembranes 40, 58-68.

arise with the use of this method. A strain gauge averages strain over its gauge length and therefore a high strain gradient will underestimate the peak tensile strain in a geomembrane. Furthermore, a strain gauge may locally stiffen the geomembrane as the stiffness of the foil, backing, and adhesive are not negligible relative to the stiffness of high-density polyethylene. As a result, only 60-80% of the actual strain may be measured with an electrical foil gauge affixed to high-density polyethylene (e.g., Brachman et al., 2000). The reliable use of strain gauges on high-density polyethylene requires calibration of every gauge under known strain conditions, which in many cases is very challenging. For these reasons, strain gauges were not used in the tests presented in this paper. The second approach to obtain strains in a geomembrane is to calculate the strains based on the deformed shape of a geomembrane (Saathoff and Sehrbrock, 1994; Dixon et al., 1997; Gallager et al., 1999; Zanzinger, 1999; Tognon et al., 2000; Gudina and Brachman, 2006; Hornsey and Wishaw, 2012). Thin lead sheets can be placed beneath the geomembrane to preserve the final deformed shape. A laser scanner can then be used to measure the deformed geomembrane surface. The assumptions made when calculating strains from the measured deformations are key to the success of this approach.

For a deformed shape with central deflection y over diameter b, as illustrated in Fig. 2.2a (where r is the radial direction and z is the vertical direction), the simplest approach to calculate strain is to: i) assume that the displacements are small (i.e., y << b) and ii) assume that the strain is uniformly distributed over the deformed shape. Then, with the assumption of either a circular or parabolic deformed shape, the radial strain ε_{arc} can be approximated through the arc elongation method as (Giroud, 1995):

$$\varepsilon_{arc} \approx 8/3\,(y/b)^2 \qquad [1]$$

Tognon et al. (2000) developed a method that explicitly considers the membrane and bending components of strain. While membrane strain is uniform throughout the thickness of the

geomembrane, bending strain varies from zero at the middle surface of the geomembrane to being greatest at the extreme fibres. This approach allows the strains to vary along the deformed surface and relaxes the need to assume a particular deformed shape, as a polynomial function is matched to the measured deformed shape. Then using finite-difference approximations, the membrane ε_M and bending ε_B components of strain are calculated using thin-shell theory as (Tognon et al., 2000):

$$\varepsilon_M = \sqrt{\left(1 + \left(\frac{1}{2\Delta r}[z_{i+\Delta r} - z_{i-\Delta r}]\right)^2\right)} - 1 \qquad [2]$$

$$\varepsilon_B = \frac{h}{(\Delta r)^2}[z_{i+\Delta r} - 2z_i + z_{i-\Delta r}] \qquad [3]$$

where: z_i, $z_{i+\Delta r}$, and $z_{i-\Delta r}$ = vertical displacements at points i, i + Δr, and i – Δr as shown in Fig. 2.2b; Δr = step increment; and h = distance from the middle surface of the geomembrane to the extreme fibre. The resulting strains at the bottom and top surfaces of the geomembrane are given as:

$$\varepsilon_{M+B} = \varepsilon_M \pm \varepsilon_B \qquad [4]$$

Hornsey and Wishaw (2012) calculated local strain by using simple trigonometry to compare the original and deformed length of a small segment along the deformed shape as:

$$\varepsilon = \frac{\sqrt{L^2 + \Delta z^2}}{L} - 1 \qquad [5]$$

where: L = the original length of the small segment; and Δz = the difference in vertical displacement over the length of the segment. In Fig. 2.2b, if L is taken as 2Δr , then Δz = $z_{i+\Delta r}$ – $z_{i-\Delta r}$, and the equation used by Hornsey and Wishaw (2012) is the same as the membrane component of strain (i.e. Eq. 2) in the thin shell theory developed by Tognon et al. (2000).

It is postulated here that the most significant assumption of the methods developed by Tognon et al. (2000) and Hornsey and Wishaw (2012) is that there are only vertical displacements and no radial displacements of the geomembrane (either away from, or towards, the centre of the indentation), as illustrated by the vertical displacement trajectories of three points in Fig. 2.2b.

Tensile strain in a geomembrane could also be calculated using the large displacement formulation of the fundamental strain-displacement relationships, provided that the magnitude and distribution of all displacement components are known. For the cylindrical coordinate system defined in Fig. 2.3, the radial strain ε_r will be the in-plane strain quantity of interest here and is defined as (e.g., see Boresi and Chong, 2000; Prager, 1973):

$$\varepsilon_r = \frac{\partial u_r}{\partial r} + \frac{1}{2}\left[\left(\frac{\partial u_r}{\partial r}\right)^2 + \left(\frac{\partial u_\theta}{\partial r}\right)^2 + \left(\frac{\partial u_z}{\partial r}\right)^2\right] \qquad [6]$$

where: r, θ, and z define the radial, tangential, and vertical directions; and u_r, u_θ and u_z are the components of displacement in the radial, tangential, and vertical directions. For the conditions of radial symmetry shown in Fig. 2.3, the tangential displacements u_θ are equal to zero and thus the radial strain is given as:

$$\varepsilon_r = \frac{\partial u_r}{\partial r} + \frac{1}{2}\left[\left(\frac{\partial u_r}{\partial r}\right)^2 + \left(\frac{\partial u_z}{\partial r}\right)^2\right] \qquad [7]$$

Using existing laser scanning techniques to obtain the vertical displacement profile (e.g., Gallagher et al., 1999; Tognon et al., 2000), the remaining task in this approach is to measure the radial displacements that may develop.

The objective of this chapter is first, to present an experimental technique to measure the radial component of displacement beneath an idealized gravel particle. Second, these results are used to investigate how significant radial displacements may be to local geomembrane strains calculated using large strain-displacement theory and how probe shape

influences the maximum calculated strains. The third objective is to compare strains calculated using large strain-displacement theory with previously used thin shell and arc elongation methods.

2.2 Method

2.2.1 Measurement of radial displacements

The approach used to measure radial displacements beneath an indentation involved tracking the location of targets affixed to the bottom surface of the geomembrane with a laser scanner. Consequently, no material was present beneath the geomembrane in these physical models, although the effect of a soft clay subgrade beneath the geomembrane on radial displacements is examined later in Section 2.4.2. A schematic of the test arrangement is shown in Fig. 2.4. Geomembrane specimens with a diameter of 60 mm were loaded using one of three machined steel probes (see Fig. 2.5) that were subjected to a prescribed vertical displacement. A line-laser capable of simultaneously tracking a 50-mm-wide zone to an accuracy of ± 0.055 mm was placed beneath the geomembrane to record both the vertical and radial positions of the targets.

A target of simple geometry which protruded slightly from the geomembrane was considered to be ideal. After several trials, stainless steel pin heads with a diameter of 1.75 mm and a height of 0.6 mm were selected. The targets were lightly pressed by hand into the geomembrane with a diameter and depth of penetration of 0.65 mm and 0.6 mm respectively, which was done to ensure that they did not fall out during testing. Fig. 2.6a depicts laser scanned profiles of the deformed shape of a geomembrane subjected to the round probe. These sorts of deformed shapes were recorded for every 1 mm of prescribed vertical displacement, although for clarity, results are shown in Fig. 2.6 only for every 4 mm of prescribed displacement. The targets, characterized by small protrusions, can clearly be seen in

each profile as the geomembrane deforms. A procedure was then developed to track the location of the centroid of each target, thus enabling the displacement trajectories to be plotted as depicted in Fig. 2.6b.

Trials were run with both the pins tracked by the laser and without pins, where the radial displacements were obtained by tracking small paint marks on the geomembrane using a photogrammetric method. No discernible difference in radial displacement was found with or without the pins, thereby suggesting that the insertion of the targets themselves did not alter the deformed shape of the geomembrane.

2.2.2 Test details

As shown in Fig. 2.4, the geomembrane was gripped and loaded in a cylindrical, stainless steel test apparatus developed by Sabir and Brachman (2012). The use of mechanical grips ensured zero radial and vertical displacement boundaries around the perimeter of the geomembrane specimen. The inside diameter of 60 mm corresponds to the mean spacing between gravel particles for nominal 50-mm coarse gravel overlying a geomembrane (Brachman and Gudina, 2008). For example, such coarse gravel meets the requirements of municipal solid waste landfill regulations in the province of Ontario (Ont. MOE, 1998).

One particular 1.5-mm-thick, smooth, high-density polyethylene geomembrane was tested. Each geomembrane specimen was obtained from the same roll for consistency. Its index properties have been reported by Sabir and Brachman (2012). The geomembrane was not punctured in any of the tests reported in this paper. A nonwoven, needle-punched geotextile (560 g/m^2) was placed on top of the geomembrane for all tests involving the cone tip in order to prevent short-term puncture.

Rather than using real gravel particles, the geomembrane was deformed by subjecting a machined steel probe to a prescribed vertical displacement. Round, cone, and flat probes were

tested and are shown in Fig. 2.5. These geometries were selected to provide idealizations of the common particle shapes in contact with the geomembrane from nominal 50 mm coarse gravel as documented by Brachman and Gudina (2008a). Use of these idealized probes rather than real gravel is advantageous in this first attempt to quantify the radial displacements beneath a gravel indentation, although their use may underestimate the strains induced by more angular gravel particles. All three probes tested were made of hardened steel and no damage or change in geometry of the probes was observed after any of the tests.

Sabir and Brachman (2012) have demonstrated that the apparatus shown in Fig. 2.4 with the round machined steel probe shown in Fig. 2.5 was able to reproduce the average geomembrane strains from real 50-mm coarse gravel obtained from 0.6-m-diameter physical experiments reported by Brachman and Gudina (2008a) when soft, compacted clay was the subgrade beneath the geomembrane.

After the materials were placed in the apparatus, vertical displacement was prescribed to the probe at a rate of 10 mm/min at 22±1°C with a maximum displacement set to 16 mm. The advantage of prescribing displacement over applying force is that the resulting strains are less sensitive to rate and temperature effects. An indication of the effects of time and temperature on local geomembrane strains under constant force can be obtained from Sabir and Brachman (2012).

2.3 Results

2.3.1 Radial displacements with round probe

Displacement trajectories for a typical test with the round probe are shown in Fig. 2.6b. It is evident that while the deformations are predominately vertical, small radially outward displacements can also be seen for targets placed away from the centre of the probe as the vertical displacement at the centre increases to 16 mm.

Plots of the radial u_r and vertical u_z components of displacement of the target centroids from the round probe at prescribed displacements of 5, 10, and 16 mm are given in Fig. 2.7. Data points from $-30 < r < 0$ mm were superimposed onto data from $0 < r < 30$ mm to get a larger data set. In general, the magnitude of radial displacement increased as vertical displacement increased. The maximum radial displacement was no larger than 10% of the maximum vertical displacement and the location of maximum radial displacement was increasingly further away from the centre of the round probe with increasing vertical displacement.

Six replicate tests were conducted at prescribed vertical displacements of 5 and 10 mm while five replicate tests were carried out at 16 mm for the round probe to provide a sense of reproducibility of the radial displacement measurements. The variability of the measured displacement components for one target location at $r = 8$ mm is given in Table 2.1. The coefficient of variation decreases for both radial and vertical components as the prescribed vertical displacement increases. Greater precision was achieved for the vertical u_z displacement component with a coefficient of variation of only 2% at a prescribed displacement of 16 mm compared to 7% for the radial u_r displacement component. Radial displacements were expected to be small and hence more sensitive to measurement error. The impact on uncertainty in measured displacements on calculated strain is provided in the following section.

2.3.2 Calculated strain with round probe

Calculated strains at prescribed displacements of 5, 10, and 16 mm with the round probe are shown in Figs 2.8a-c. In all plots, tensile strain is taken as positive. Strains calculated using the large strain-displacement formulation of Eq. 7 are denoted as ε_r and are plotted as solid lines. These were found by fitting polynomial functions to the measured displacements (the solid lines plotted in Fig. 2.7) and then computing the derivatives of those functions as per Eq. 7. At

each magnitude of prescribed vertical displacement, the large strain-displacement formulation calculates the maximum strain beneath the centre of the round probe (i.e., at r = 0 mm). Maximum strain values of 15, 25, and 44% were calculated at prescribed displacements of 5, 10, and 16 mm as shown in Figs 2.8a-c.

The relative magnitudes of the three components of the large strain-displacement equation, Eq. 7, at a prescribed displacement of 16 mm are shown in Fig. 2.8d where it can be seen that the maximum strain is primarily dictated by the first term of Eq. 7, $\partial u_r/\partial r$, as it contributes a strain of 37% to the maximum total strain of 44%. Although u_r is small relative to u_z, its rate of change with respect to r (i.e., the slopes of the plots in Figs 2.7a-c) governs the maximum calculated strain in this case. The magnitude of the second term of the large strain-displacement equation, $\frac{1}{2}(\partial u_r/\partial r)^2$, is 7% strain at r = 0, which slightly increases the maximum calculated strain. The third term, $\frac{1}{2}(\partial u_z/\partial r)^2$, has no contribution to the strain beneath the probe because the rate of change of u_z with respect to *r* approaches zero at this location (Fig. 2.7f). This third term does calculate tensile strains along the side slope of the indentation (with its greatest value occurring around r = 16 mm) as depicted in Fig. 2.8d.

It is tempting in many engineering mechanics problems to assume small displacements, such that higher order terms in the large strain-displacement equation (i.e., second and third terms in Eq. 7) are negligibly small. In this particular problem, assuming small displacements would result in a maximum strain of 37% compared to 44% with large strain-displacement theory at 16 mm of prescribed displacement. However, this assumption would unrealistically predict compression in the zone where r > 10 mm as depicted in Fig. 2.8d. Large strain-displacement theory is therefore required for this problem even at displacements as small as 5 mm.

The impact of uncertainty in measured radial displacements on the resulting strain calculations is shown in Table 2.2. These values were obtained by fitting upper and lower bound

trends through the measured u_r data, where the bounds were obtained using the 95% confidence interval on the mean. At a prescribed displacement of 10 mm, the estimate of mean strain is 25% ± 3% strain. At this magnitude of displacement, a coefficient of variation of 11% in u_r results in a similar level of uncertainty with the estimate of mean strain also to ± 11% of the mean value. However, uncertainty in u_r has a greater impact on strain calculations at a prescribed displacement of 16 mm where the estimate of mean strain is 42% ± 7% strain. Despite a coefficient of variation of 7% in u_r measurement, the estimate of radial strain is within ± 17% of the mean value. Uncertainty in u_r has a greater impact on slope (i.e., $\partial u_r/\partial r$) and thus a greater uncertainty in the calculation of mean strain at larger displacements. For the remainder of the paper, maximum strains are reported as the largest (in terms of their radial distribution) of the mean values based on the replicate tests.

2.3.3 Influence of probe shape

Typical displacement trajectories with the cone probe are plotted in Fig. 2.9. Comparison with the round probe trajectories plotted in Fig. 2.6b show greater outward radial displacements with the cone probe. Perhaps even more importantly, the maximum radial displacement occurs closer to the centre of the probe with the cone (see Fig. 2.10) than for the round probe. This would lead to a larger $\partial u_r/\partial r$ term for the cone probe and higher calculated strains with the cone as plotted in Fig. 2.11.

At a prescribed displacement of 5 mm (Fig. 2.11a), the maximum strain with the cone probe is 2 times greater than that with the round probe. The impact on maximum strain is even more apparent at larger displacements. At prescribed displacements of 10 and 16 mm (Figs 2.11b & 2.11c), the maximum strain calculated with the cone probe is around 3 times larger than the round probe. Intuitively, it was expected that the cone probe would be worse in terms of short-term geomembrane puncture because of its much sharper tip, but the difference in probe

shape also produces more significant radial displacements and thus has a large impact on tensile strains. Thus, in addition to puncture potential from the sharp cone probe, there is also much greater tensile elongation near the centre of the probe.

Separation of the three strain components of Eq. 7 in Fig. 2.11d shows the large computed values from the $\partial u_r/\partial r$ term. Since this first term is so large, the higher order second term, $½(\partial u_r/\partial r)^2$, also contributes a significant proportion of the maximum strain. Fig. 2.11d also shows that much like for the round probe, the third component related to the vertical displacements does not contribute to the maximum strain located directly beneath the probe.

The displacement trajectories with the flat probe are plotted in Fig. 2.12. The deformations are predominantly vertical directly beneath the flat probe ($-12.5 < r < 12.5$ mm), with an abrupt change in vertical displacement just away from the edge of the flat probe (i.e. at $|r| > 12.5$ mm). Radial displacements are also evident just away from the edge of the flat probe. The resulting radial and vertical components of displacement are plotted in Fig. 2.13.

Calculated strains with the flat probe are given in Fig. 2.14. Unlike the round and cone probes, the maximum strain with the flat probe is not located at the centre but rather near the edge of the probe. This is because the rate of change in both u_r and u_z with respect to r is small beneath the flat probe; however, both components reach a maximum near the edge of the probe leading to maximum strains at this location. Fig. 2.14d shows that the third term of Eq. 7, $½(\partial u_z/\partial r)^2$ which is a function of the vertical deflections, dominates the maximum calculated strain at a prescribed displacement of 16 mm. Given the very large gradient in vertical and radial displacements just beside the edge of the flat probe at a prescribed displacement of 16 mm (see Figs 2.13c & 2.13f), the flat probe resulted in the largest strain of the three probes tested with a maximum strain of nearly 180% strain, relative to 125% strain from the cone and 44% strain from the round probe (e.g., see Figs 2.8c, 2.11c, & 2.14c).

The influence of probe shape on the maximum calculated strain for prescribed vertical displacements with more realistic values that are less than 10 mm is shown in Fig. 2.15. For these displacements, the flat probe resulted in the smallest strains and the cone with the largest. For example, at a prescribed vertical displacement of 4 mm, the maximum strain from the round probe of 13% was nearly 4 times larger than the strain from the flat probe, while the strain from the cone of 22% was approximately 6 times larger than that with the flat probe.

2.4 Discussion

2.4.1 Comparison with other strain calculation methods

Strains calculated using thin shell theory given by Eqs 2-4 from Tognon et al. (2000) are also plotted for the three probes in Figs 2.8, 2.11, and 2.14 denoted as ($\varepsilon_M + \varepsilon_B$) with the dashed lines. Relative to large strain-displacement theory, thin shell theory provides a much different distribution of strain for both the round and cone probes as illustrated in Figs 2.8 & 2.11. The most significant difference between the two strain calculation methods is directly beneath the probe where large strain-displacement theory calculates strains to be a maximum, whereas thin shell theory calculates strains that are 4-6 times smaller for the round probe and 8-12.5 times smaller for the cone probe. These strain calculations at r = 0 are summarized in Table 2.3. This difference arises from the unstated - but implicit - assumption by Tognon et al. (2000) that the geomembrane experiences vertical displacements only (i.e., $u_r = 0$ as illustrated in Fig. 2.2b). Not only does thin shell theory underestimate the maximum strain, but it also unrealistically calculates compression beneath the probe on the top surface of the geomembrane – see the ($\varepsilon_M - \varepsilon_B$) values in Table 2.3 – because of the bending component of strain (Eq. 3). In terms of strain from the vertical displacement component, the membrane component of strain from the thin shell method (Eq. 2, Fig. 2.8e) essentially provides the same results as the third component of the large strain-displacement theory plotted in Fig. 2.8d for the round probe.

For the flat probe, where the maximum strain was not located directly beneath the probe but more influenced by the rate of change in the vertical component of displacement, the thin shell calculations of maximum strain match quite well with the large strain-displacement approach for prescribed displacements less than 10 mm, as can be seen in Figs 2.14a & 2.14b and as summarized in Table 2.4. However, for the prescribed displacement of 16 mm in Fig. 2.14c, the thin shell approach provides strains that are less than one-third of the maximum strain from the large strain-displacement approach.

There is some data that suggests that it is not just puncture directly beneath the tip of gravel contacts that may be of concern, but that rupture from excessive tensile strain mid-way along the side slopes of the deformed shape may also warrant evaluation (e.g., see Gudina 2007, Sabir 2011). For the round probe, strain at this location ($10 < r < 20$ mm, in Fig. 2.8d) is dominated by the $½(\partial u_z/\partial r)^2$ term and the rate of change in u_r is small enough that the assumptions inherent in the method of Tognon et al. (2000) are more valid at the side slopes than at the centre of the deformed shape. The maximum calculated strains along the side slope of the deformed geomembrane are given in Table 2.4. At this location, thin shell theory calculates strains for the round probe that are 2.0 and 1.3 times larger than large strain-displacement theory at prescribed displacements of 10 and 16 mm respectively. Thin shell theory is in much closer agreement with large strain-displacement theory at $10 < r < 20$ mm for the round probe.

Geomembrane strain was also calculated using the arc elongation method given by Eq. 1. Since this method simplistically assumes strain is uniformly distributed along the deformed shape, it makes sense that it would underestimate the maximum strain relative to the large strain-displacement approach. Taking b as the width of the deformed shape (60 mm), as shown in Fig. 2.2, the results from this method are also given in Tables 2.3 and 2.4. For the round probe, the arc elongation method underestimates peak strain by factors between 8-2 for

prescribed displacements of 5-16 mm. This method makes no provision for local strain variations from probe shape. Therefore, the calculated strains for both the cone and flat probes are the same as calculated for the round probe. As a result, the arc elongation method underestimates the maximum strain with the cone probe by factors between 16-7 at vertical displacements of 5-16 mm (Table 2.3). Results are nearly as poor for the case of the flat probe.

2.4.2 Impact of clay beneath the geomembrane

When a material such as clay is placed beneath the geomembrane, the approach shown in Fig. 2.4 clearly cannot be used to track the radial component of displacement. A method developed to measure radial displacements for the case of clay beneath the geomembrane is illustrated in Fig. 2.16. Here, ink-mark targets were drawn on the bottom surface of the geomembrane at a 2.5 mm centre-to-centre spacing. An initial photograph (taken with an 18 MB digital single-lens reflex camera) and profile with the line-laser of the bottom surface of the geomembrane were taken prior to running the test as depicted in Fig. 2.16a. A 50-mm-thick layer of compacted silty-clay (with particles greater than 10 mm in diameter removed) was then placed in the bottom half of the test apparatus and compacted to a dry density of 1.9 g/cm^3 and a water content of 16%. These values correspond to its Std Proctor maximum dry density and 4% wet of its Std Proctor optimum water content and correspond to the upper practical limit of water content for this particular low plasticity silty-clay as a compacted clay liner in field applications (e.g., see Rowe et al. 2004). A very thin sheet of plastic film was placed between the geomembrane and the compacted clay to minimize disturbance of the targets. After the geomembrane was clamped in place, a prescribed displacement of 14 mm was applied to the round probe lowered at a rate of 10 mm/min. Once 14 mm of vertical displacement was achieved, the force was held constant and the top portion of the test apparatus was filled with grout and allowed to set for 30 minutes to preserve the deformed geomembrane surface (Fig.

2.16b). A final photograph and profile with the line-laser of the bottom surface of the geomembrane were taken after running the test (Fig. 2.16c). Vertical displacements were obtained through the profile of the deformed geomembrane surface. Radial displacements were measured through photogrammetric tracking of the ink marks between the initial and final photos. The resolution of the digital images in this trial was such that radial displacements were obtained to within ±0.025 mm.

A comparison of radial and vertical components of displacement and calculated strains at 14 mm of prescribed vertical displacement for the cases of clay and no clay beneath the geomembrane are shown in Fig. 2.17. Both radial and vertical displacements for the two cases are in close agreement. The maximum tensile strain in the geomembrane with clay and no clay beneath the geomembrane was 36 and 38% respectively. Thus, there is no discernible difference in radial displacements or maximum calculated tensile strain whether air or soft clay is beneath the geomembrane, for the particular conditions tested.

2.4.3 Practical implications

Tensile strains which can develop in a geomembrane need to be quantified when assessing if a specific protection layer is able to limit those strains to an acceptable level for a given type of gravel, geomembrane, subgrade, pressure, temperature, chemical exposure, and time. The principle advantage of the new method proposed in this paper is that no simplifying assumptions are required in terms of the distribution of strain or the mode of deformation. However, while calculating strain from radial displacements is straightforward, their measurement is not. This is made even more challenging when dealing with real gravel (e.g., Brachman and Gudina, 2008a), as opposed to a single machined steel probe where radially symmetric conditions prevail. The location and size of real gravel varies and so it would be difficult to locate targets beneath the location of significant indentations.

When assessing geomembrane strain right beneath the centre of the probe (r = 0 mm), thin shell theory or any other method that neglects radial displacements will not provide a precise calculation of strain and should therefore be viewed as an index value. Quantifying strain along the side slopes of the indentation may also be an important consideration due to the potential for rupture. At this location (10 < r < 20 mm) thin shell theory and large strain-displacement theory were in close agreement for the case of the round probe since vertical displacements dominate strain along the indentation sides. By assuming only vertical displacements, strain can be calculated using thin shell theory. However, if only the strain along the side slopes of an indentation are desired, rather than requiring the finite difference solutions of Eqs 2 & 3, one could get a similar result by simply taking a polynomial fit to the vertical displacement (same as the first step required for thin shell theory) and computing the maximum value of $1/2(\partial u_z/\partial r)^2$. Regardless of the location in which strain is being calculated, it is clear that the limiting strain and the method used to calculate that strain must be specified.

Uncertainty must be recognized and taken into consideration when assessing tensile strains in a geomembrane. In addition to uncertainty from material variability (dominated by irregularly spaced and shaped gravel contacts) as quantified by Brachman and Gudina (2008a), there is additional uncertainty introduced by the assumptions of the method used to compute strain (i.e. model uncertainty) as discussed in this paper. The assumption of uniform strain in the arc elongation method or of zero radial displacement in thin shell theory results in significant model uncertainty. While large strain-displacement theory does not incorporate the underlying assumptions of uniform strain or zero radial displacement, it is also prone to uncertainty arising from measurement accuracy, particularly for the radial component of displacement and curve fittings used, as quantified in this paper.

Last, some insight into the displacement required to reach proposed allowable strain limits for high-density polyethylene geomembranes can be gained from the reported strains. For

reference, Seeger and Müller (2003) have proposed one limit of 3%, while Peggs et al. (2005) have proposed another of 6-8%. Vertical displacements beneath the centre of the probe at r = 0 required to reach these proposed limits are given in Table 2.5. They depend on probe shape and size and the position where the allowable strain is evaluated. For both the round and cone probes, as little as 1 to 2 mm of vertical displacement is sufficient to reach strains of 3 to 6% if limited by the maximum strain, which for these shapes occurred at the centre. As shown in Fig. 2.15, there is very little difference between the round and cone probes at these small displacements. If the tensile strains for these probes are limited by the strains along the side slope of the indentation, the allowable displacements then increase to 8 to 13 mm. For the flat probe, strains of 3 and 6% are reached at vertical displacements of 4 and 6 mm. It is clear that for the particular conditions tested, strain limits were reached at remarkably small vertical displacements. This is consistent with results from larger-scale protection layer testing with 50-mm coarse gravel above a 1.5-mm-thick high-density polyethylene geomembrane where only thick soil layers have been shown to limit the tensile strains to very small levels (< 2%) at vertical pressures up to 1000 kPa (Tognon et al. 2000; Gudina and Brachman, 2006; Brachman and Gudina, 2008b; Dickinson and Brachman, 2008). While it is not yet clear to what value and at what location the strains should be limited, it is apparent that in addition to the method of calculation, the location at which strain is being calculated can have a significant impact on strain assessment.

2.5 Conclusions

An experimental technique to measure the radial and vertical components of geomembrane displacement from gravel indentations was presented. Short-term physical experiments were conducted where vertical displacement was prescribed to a 60-mm-diameter, 1.5-mm-thick high-density polyethylene geomembrane using one of three machined steel

probes with either a round, cone, or flat tip. Measurements of vertical and radial displacements were used to calculate geomembrane strains using large strain-displacement theory. The results were used to show the importance of radial displacements on the calculated strains, to quantify the influence of probe shape on the calculated strains, and to compare the results with previously used thin shell and arc elongation calculation methods. The method of calculation and the location at which strain is being calculated were both found to have a significant impact on strain assessment. For the particular conditions examined, the principal conclusions are:

a) Importance of radial displacements: Radial displacements (u_r) at local geomembrane indentations were found to be small relative to vertical displacements (u_z), but not negligible when calculating local geomembrane strains. They were shown to provide the dominant contribution to the maximum strain beneath the centre of the round and cone shaped probes, as it is the rate of change of radial displacement away from the indentation centre (i.e. $\partial u_r/\partial r$) rather than its magnitude alone that governs the resulting strain. Neglecting radial displacements yielded strain calculations that were only 10 to 20% of the maximum strain for the round and cone probes at a prescribed vertical displacement of 5 mm.

b) Probe shape: The shape of the probe deforming the geomembrane was shown to impact both the magnitude and distribution of radial displacements, and hence the resulting maximum strain. For both the round and cone probes, the maximum strain in the geomembrane was located directly beneath the centre of the probe, while the maximum strain with the flat probe was located near the edge of the probe. At a prescribed vertical displacement of 5 mm, the round and cone probes resulted in maximum strains that were 3 and 7 times larger than that for the flat probe. At much larger displacements, the flat probe yielded the largest strain with values that were 4 times larger than with the round probe and 1.4 times larger than with the cone.

c) Comparison with other methods: Both the thin shell and arc elongation methods produced incorrect distributions of strain and also provided magnitudes that significantly underestimated the maximum geomembrane strain. While it is well understood that the arc elongation method assumes a uniform distribution of strain and hence underestimates the maximum strain beneath a gravel contact, it was shown that the thin shell method assumption of only vertical geomembrane displacements (i.e., $u_r = 0$) results in strain calculations that underestimate the maximum strain by factors of 2 to 3 for the round probe and 3 to 5 for the cone, depending on the magnitude of prescribed displacement. With the flat probe and for prescribed displacements less than 10 mm (i.e. where radial displacements were less significant) calculations of maximum strain with the thin shell method matched quite well with the large strain-displacement approach.

2.6 References

Boresi, A.P., Chong, K.P., 2000. Elasticity in Engineering Mechanics. 2ed. Wiley, New York.

Brachman, R.W.I., Moore, I.D., Rowe, R.K., 2000. Local strain on a leachate collection pipe. Canadian Journal of Civil Engineering 27 (6), 1273-1285.

Brachman, R.W.I., Gudina, S., 2008a. Gravel contacts and geomembrane strains for a GM/CCL composite liner. Geotextiles and Geomembranes 26 (6), 448-459.

Brachman, R.W.I., Gudina, S., 2008b. Geomembrane strains from coarse gravel and wrinkles in a GM/GCL composite liner. Geotextiles and Geomembranes 26 (6), 488-497.

Dickinson, S., Brachman, R.W.I., 2008. Assessment of alternative protection layers for a geomembrane / geosynthetic clay liner (GM/GCL) composite liner. Canadian Geotechnical Journal 45 (11), 1594-1610.

Dixon, N., Jones, D.R.V., Hayden, J., 1997. Performance of geoprotectors for landfill liners. Proc., Geoenvironmental Engineering Conference, Cardiff, UK, 351-356.

Gallagher, E.M., Darbyshire, W., Warwick, R.G., 1999. Performance testing of landfill geoprotectors: Background, critique, development and current practice. Geosynthetics International 6 (4), 283-301.

Giroud, J.P., 1995. Determination of geosynthetic strain due to deflection. Geosynthetics International 2 (3), 635-641.

Gudina, S., 2007. Short-term physical response of HDPE geomembranes from gravel indentations and wrinkles. PhD thesis, Department of Civil Engineering, Queen's University, Kingston, Ontario.

Gudina, S., Brachman, R.W.I., 2006. Physical response of geomembrane wrinkles overlying compacted clay. Journal of Geotechnical and Geoenvironmental Engineering 132 (10), 1346-1353.

Hornsey, W.P., Wishaw, D.M., 2012. Development of a methodology for the evaluation of geomembrane strain and relative performance of cushion geotextiles. Geotextiles and Geomembranes 35, 87-99.

Koerner, R.M., Hsuan, Y.G., Koerner, G.R., Gryger, D., 2010. Ten year creep puncture study of HDPE geomembranes protected by needle-punched nonwoven geotextiles. Geotextiles and Geomembranes 28 (6), 503-513.

Ontario Ministry of the Environment (Ont. MOE), 1998. Landfill standards: A guideline on the regulatory and approval requirements for new or expanding landfilling sites. Ontario Regulations 232/98. Queen's Printer for Ontario, Toronto.

Peggs, I.D., Schmucker, B., Carey, P., 2005. Assessment of maximum allowable strains in polyethylene and polypropylene geomembranes. Proc., Geo-Frontiers 2005, Austin, Texas (doi http://dx.doi.org/10.1061/40789(168)23).

Prager, W., 1973. Introduction to Mechanics of Continua. Dover, New York.

Rowe, R.K., Quigley, R.M., Brachman, R.W.I., and Booker, J.R., 2004. Barrier Systems for Waste Disposal Facilities. 2nd Ed., E & FN Spon, London, 587 pp.

Rowe, R.K., 2012. Short and long-term leakage through composite liners, The 7th Arthur Casagrande Lecture, Canadian Geotechnical Journal 49 (2), 141-169.

Saathoff, F., Sehrbrock, U., 1994. Indicators for selection of protection layers for geomembranes. Proc., Fifth International Conference on Geotextiles, Geomembranes and Related Products, Singapore, 1019-1022.

Sabir, A., 2011. Assessment of long-term tensile strains in HDPE geomembranes from gravel indentations. PhD thesis, Department of Civil Engineering, Queen's University, Kingston, Ontario.

Sabir, A., Brachman, R.W.I., 2012. Time and temperature effects on geomembrane strain from a gravel particle subject to sustained vertical force. Canadian Geotechnical Journal, 49 (3), 249-263.

Seeger, S., Müller, W., 2003. Theoretical approach to designing protection: selecting a geomembrane strain criterion. Geosynthetics: Protecting the Environment. Dixon, N., Smith, D.M., Greenwood, J.H., Jones, D.R.V. (Eds.), Thomas Telford, London, 137-152.

Tognon, A.R., Rowe, R.K., Moore, I.D., 2000. Geomembrane strain observed in large-scale testing of protection layers. ASCE Journal of Geotechnical and Geoenvironmental Engineering 126 (12), 1194-1208.

Zanzinger, H., 1999. Efficiency of geosynthetic protection layers for geomembrane liners: performance in a large-scale model test. Geosynthetics International 6 (4), 303-317.

Table 2.1: Variability of target data at r = 8 mm for the round probe.

Displacement Component	Prescribed Displacement	Number of data points	Mean (mm)	Standard deviation (mm)	95% Confidence Interval on mean (mm)	Coefficient of variation
u_r	5	6	0.29	0.05	0.04	0.18
	10	5	0.92	0.10	0.08	0.11
	16	6	1.70	0.11	0.09	0.07
u_z	5	6	3.21	0.19	0.15	0.06
	10	5	7.72	0.27	0.24	0.04
	16	6	13.1	0.25	0.20	0.02

Table 2.2: Upper and lower bounds on calculation of mean strain (%) for the round probe at the centre (r = 0 mm).

Prescribed displacement (mm)	Maximum strain (%)		
	Lower bound	Mean	Upper bound
10	22	25	28
16	36	42	49

Table 2.3: Summary of geomembrane strain at the centre (r = 0).

Tip	Prescribed Displacement (mm)	Strain (%)			
		ε_r Eq. 6	$\varepsilon_M + \varepsilon_B$ Eqs 2-3	$\varepsilon_M - \varepsilon_B$ Eqs 2-3	ε_{arc} Eq. 1
Round	5	15	3.5	-3.5	1.9
	10	25	6.0	-5.9	7.4
	16	44	6.9	-6.9	19
Cone	5	30	3.6	-3.6	1.9
	10	72	7.0	-7.0	7.4
	16	125	10	-10	19
Flat	5	0.0	1.1	-1.0	1.9
	10	18	1.4	-1.1	7.4
	16	15	3.0	-1.9	19

Table 2.4: Summary of geomembrane strain at the side slope.

Tip	Prescribed Displacement (mm)	Strain (%)			
		ε_r Eq. 6	$\varepsilon_M + \varepsilon_B$ Eqs 2-3	$\varepsilon_M - \varepsilon_B$ Eqs 2-3	ε_{arc} Eq. 1
Round	5	1.6	5.3	4.3	1.9
	10	7.4	15	15	7.4
	16	21	27	26	19
Cone	5	1.5	5.8	5.2	1.9
	10	3.7	19	18	7.4
	16	14	38	36	19
Flat	5	4.6	4.7	5.1	1.9
	10	21	19	19	7.4
	16	177	44	44	19

Table 2.5: Vertical displacement at r = 0 (mm) to reach proposed allowable strains.

Probe	Strain limit	Location	
		Centre (r = 0 mm)	Side slope (10 < r < 20 mm)
Round	3%	~1	8
	6%	~2	9
Cone	3%	~1	9
	6%	~2	13
Flat	3%	-	4
	6%	-	6

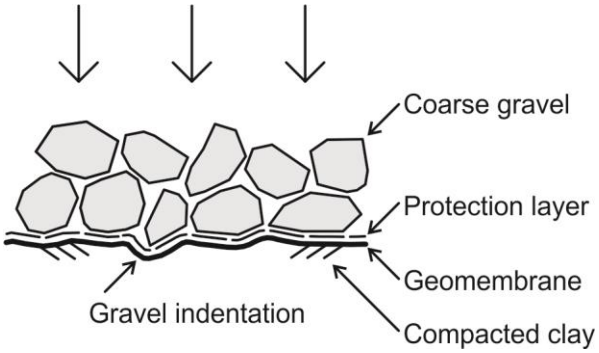

Fig. 2.1. Schematic of gravel particles leading to local indentations in a geomembrane.

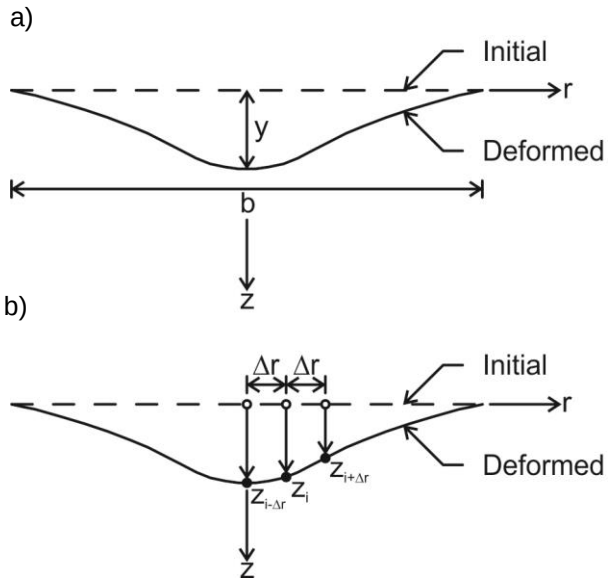

Fig. 2.2. Notation for strain calculation methods: a) arc elongation and b) thin shell theory.

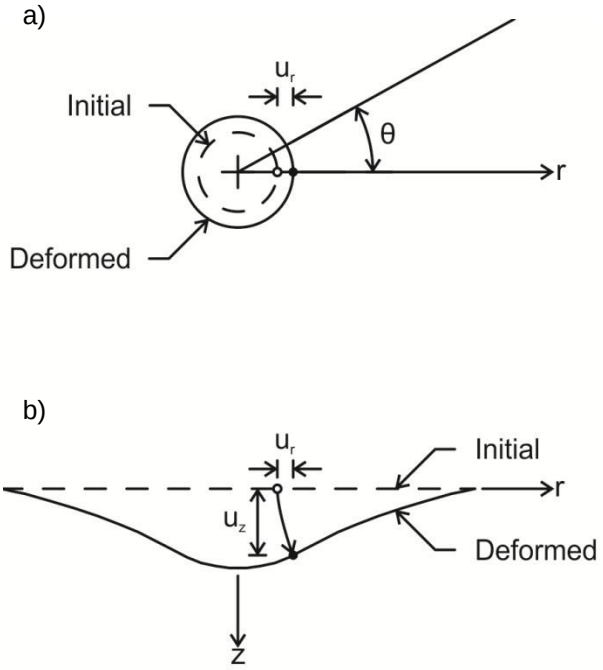

Fig. 2.3. Postulated geomembrane deformations: a) plan view and b) section view.

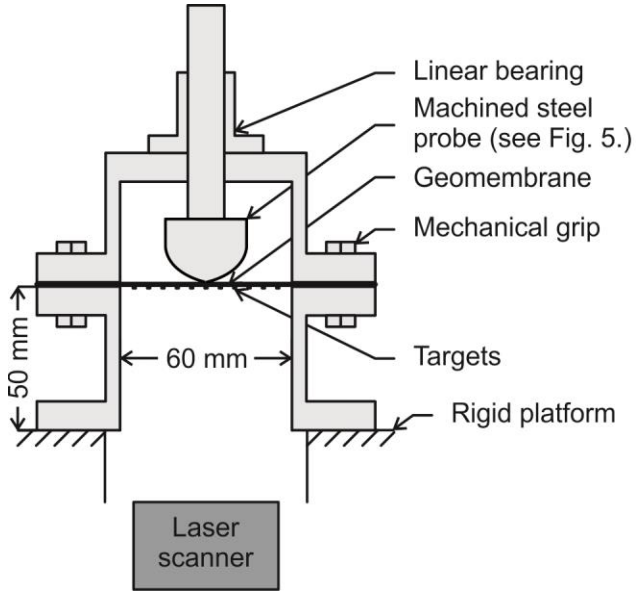

Fig. 2.4. Cross section of apparatus.

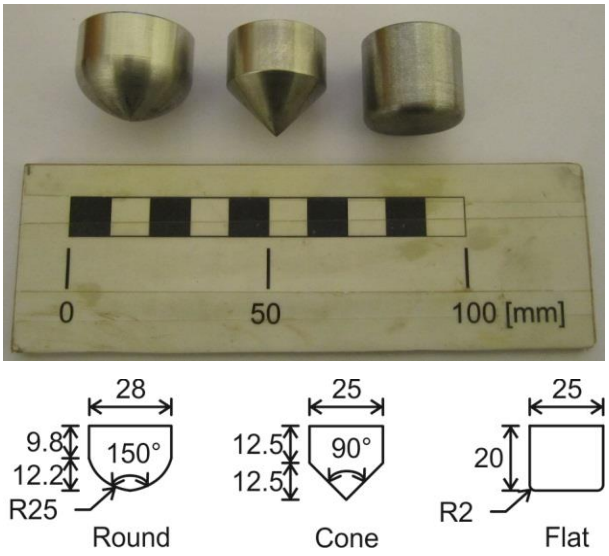

Fig. 2.5. Three probes tested. Dimensions in mm.

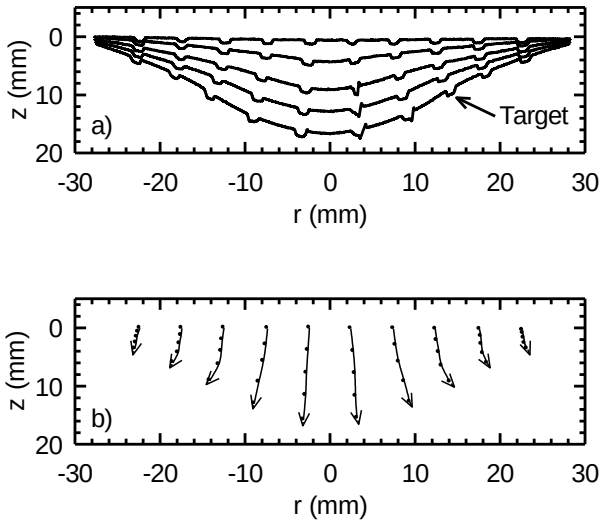

Fig. 2.6. Local indentation for a typical test with the round probe showing: a) laser scanned profiles and b) the inferred displacement trajectories at prescribed displacements of 0, 4, 8, 12, and 16 mm.

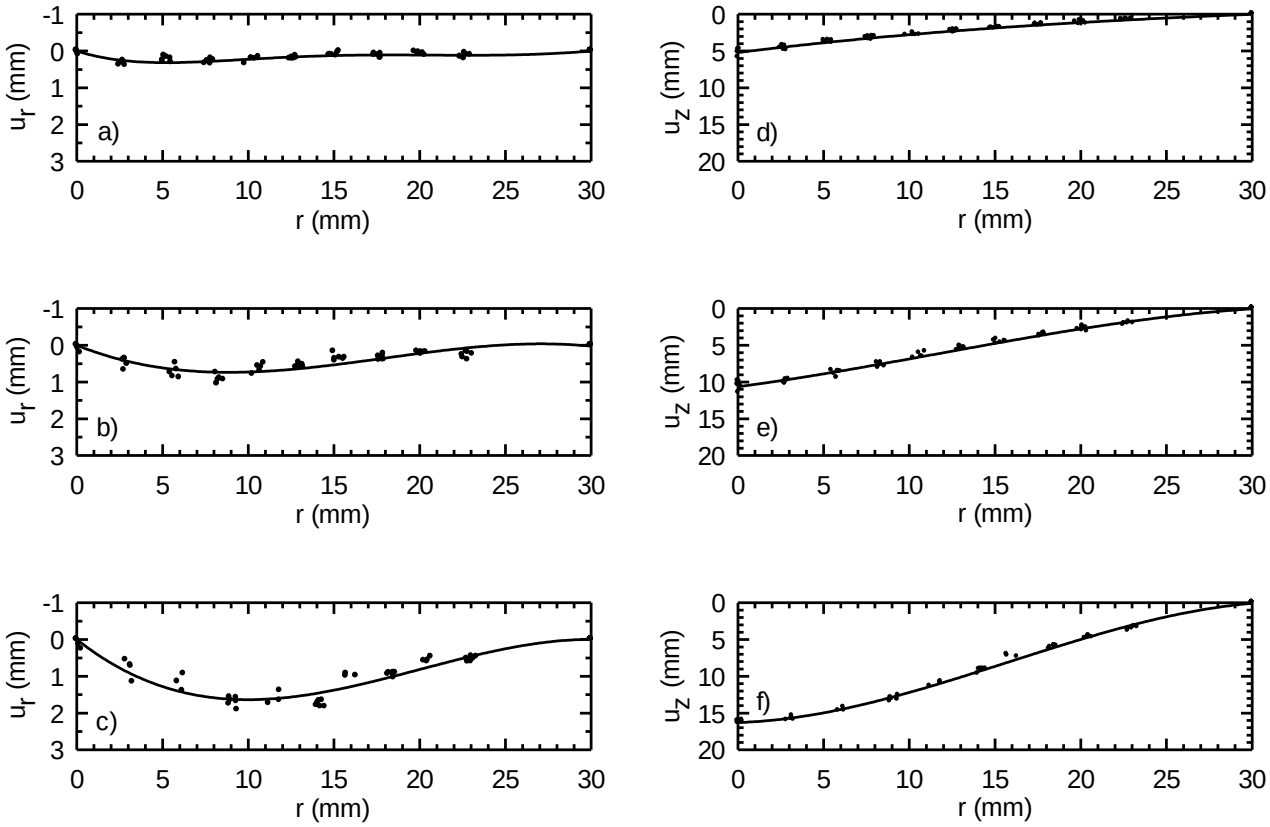

Fig. 2.7. Radial (u_r) component of displacement at prescribed displacements of: a) 5 mm, b) 10 mm, and c) 16 mm along with vertical (u_z) component of displacement at prescribed displacements of: d) 5 mm, e) 10 mm, and f) 16 mm from the round probe.

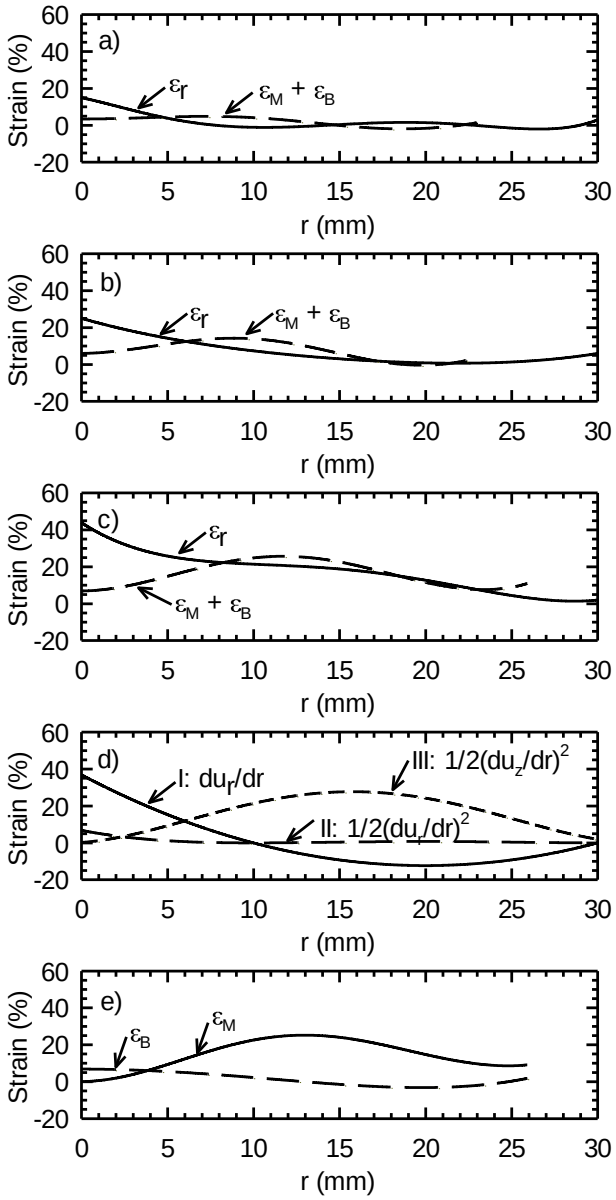

Fig. 2.8. Strains calculated using large strain-displacement formulation (ε_r) and thin shell theory ($\varepsilon_M + \varepsilon_B$) from the round probe at prescribed displacements of: a) 5 mm, b) 10 mm, and c) 16 mm along with d) the components of large strain-displacement formulation for 16 mm of displacement and e) the membrane (ε_M) and bending (ε_B) strains from thin shell theory for 16 mm of displacement.

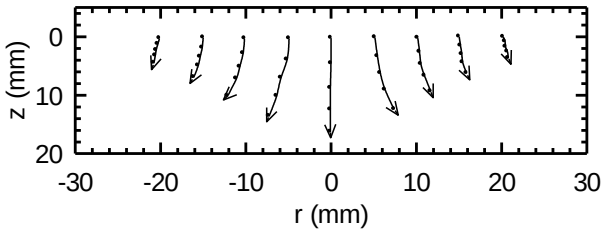

Fig. 2.9. Inferred displacement trajectories from a typical test with the cone probe at prescribed displacements of 0, 4, 8, 12, and 16 mm.

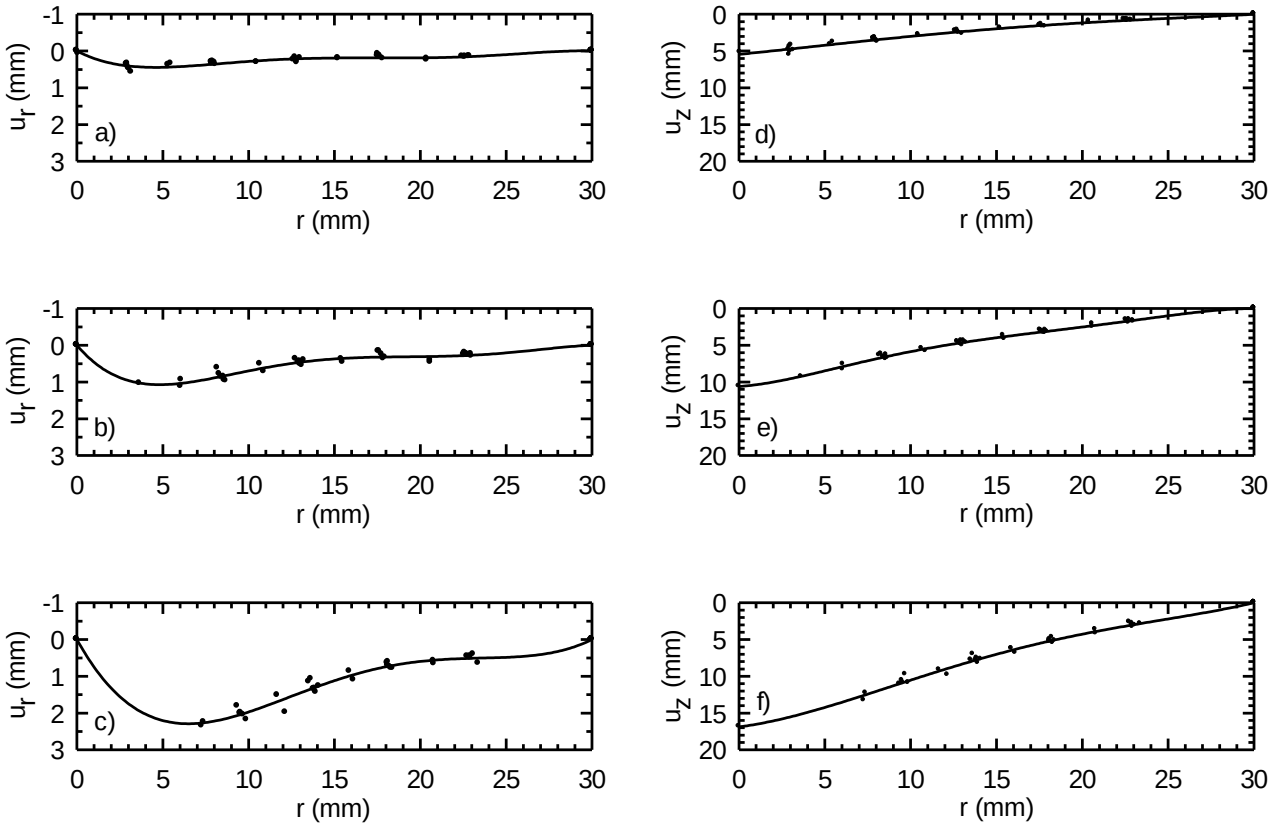

Fig. 2.10. Radial (u_r) component of displacement at prescribed displacements of: a) 5 mm, b) 10 mm, and c) 16 mm along with vertical (u_z) component of displacement at prescribed displacements of: d) 5 mm, e) 10 mm, and f) 16 mm from the cone probe.

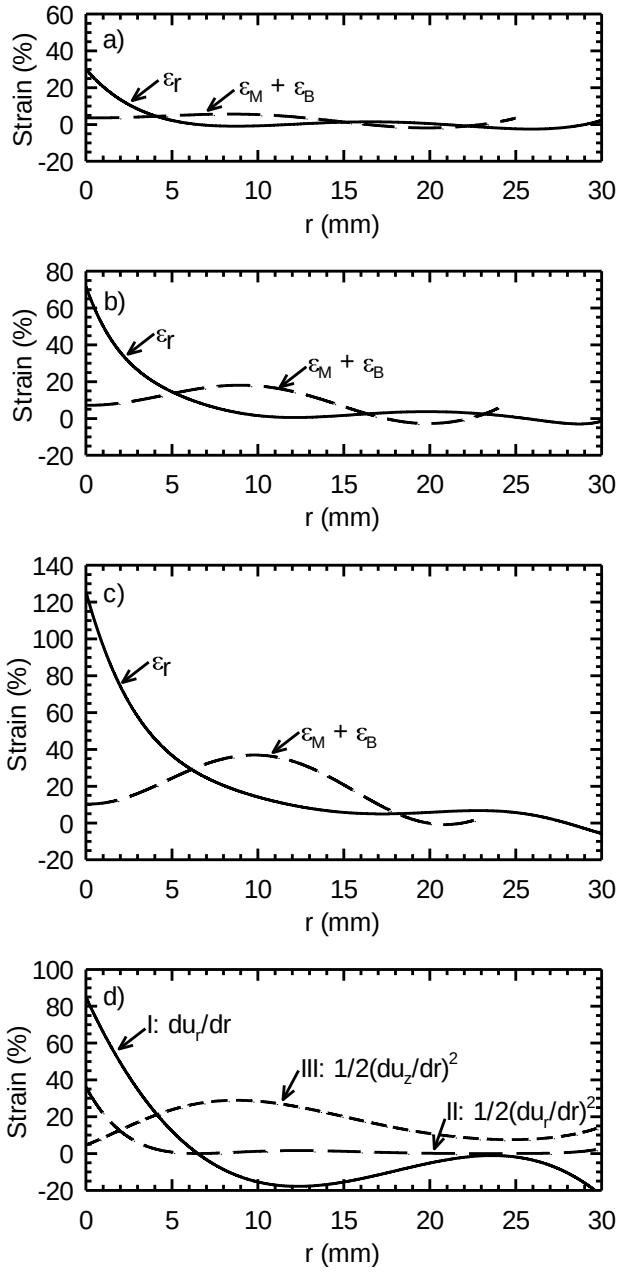

Fig. 2.11. Strains calculated using large strain-displacement formulation (ε_r) and thin shell theory ($\varepsilon_M + \varepsilon_B$) from the cone probe at prescribed displacements of: a) 5 mm, b) 10 mm, and c) 16 mm along with d) the components of large strain-displacement formulation for 16 mm of displacement.

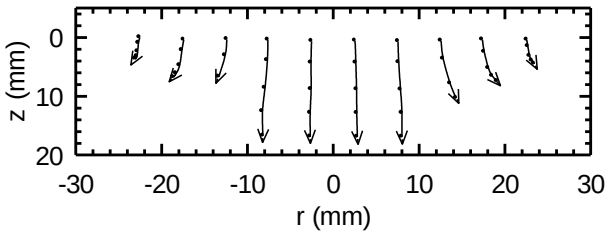

Fig. 2.12. Inferred displacement trajectories for a typical test with the flat probe at prescribed displacements of 0, 4, 8, 12, and 16 mm.

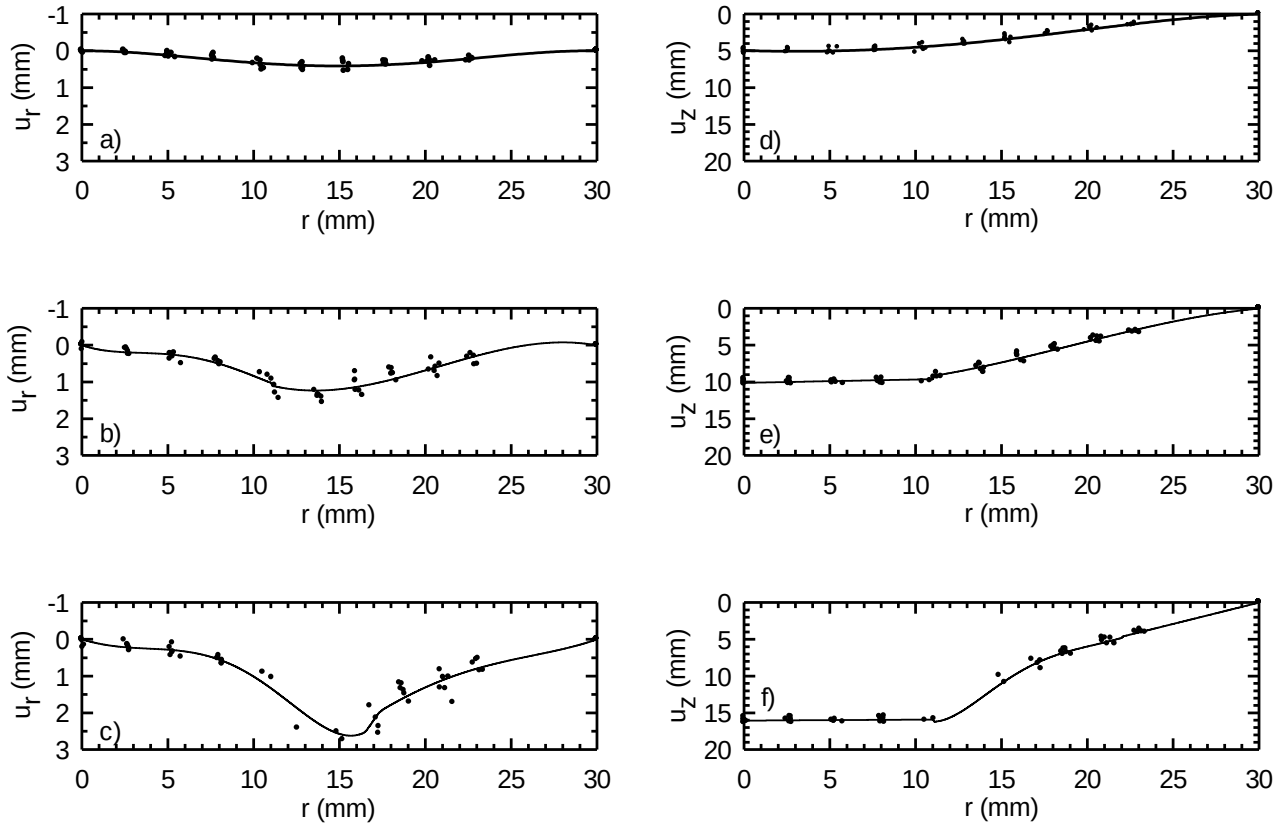

Fig. 2.13. Radial (u_r) component of displacement at prescribed displacements of: a) 5 mm, b) 10 mm, and c) 16 mm along with vertical (u_z) component of displacement at prescribed displacements of: d) 5 mm, e) 10 mm, and f) 16 mm from the flat probe.

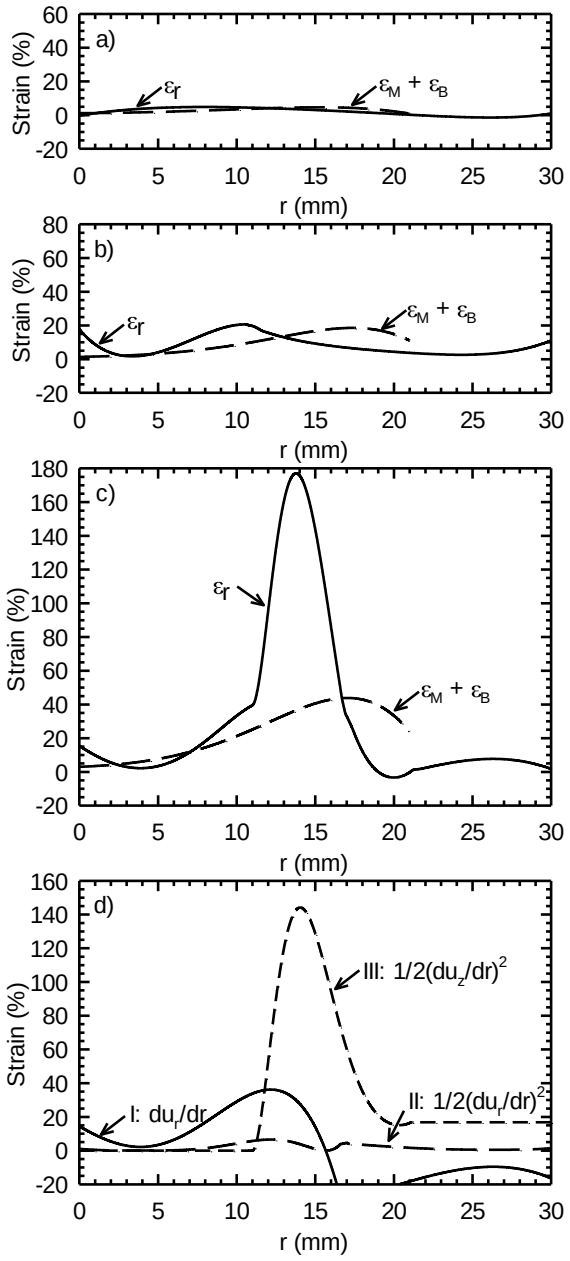

Fig. 2.14. Strains calculated using large strain-displacement formulation (ε_r) and thin shell theory ($\varepsilon_M + \varepsilon_B$) from the flat probe at prescribed displacements of: a) 5 mm, b) 10 mm, and c) 16 mm along with d) the components of large strain-displacement formulation for 16 mm of displacement.

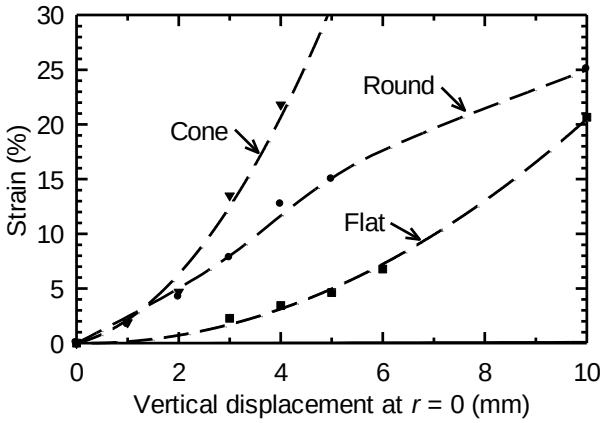

Fig. 2.15. Maximum strain with the round, cone, and flat probes.

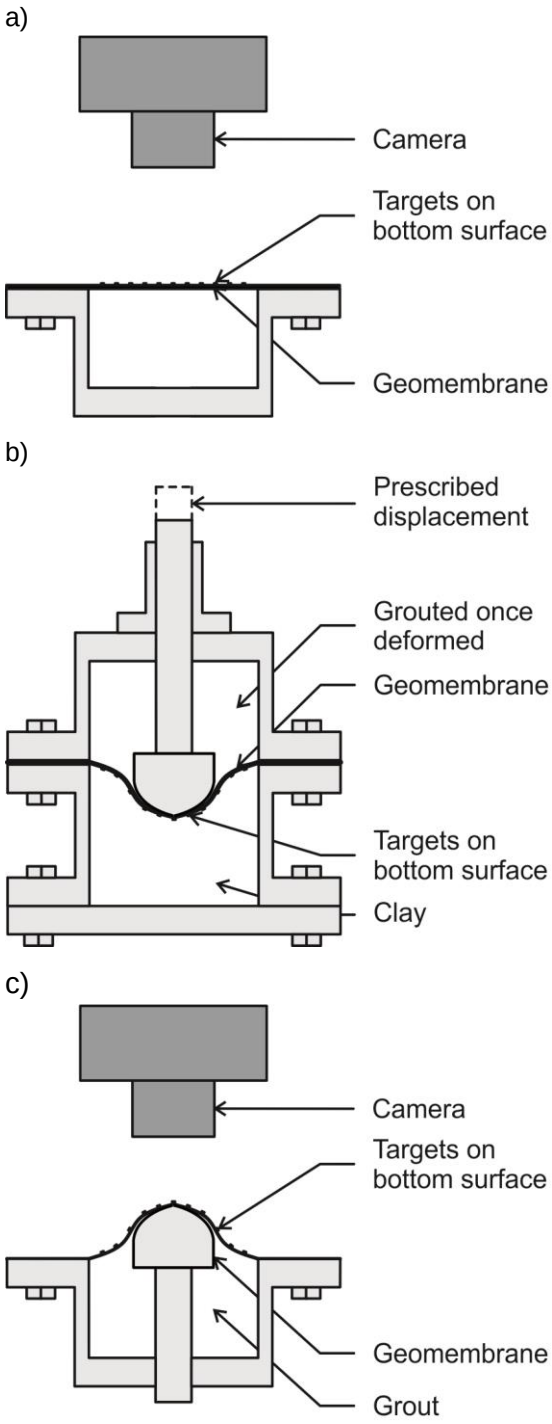

Fig. 2.16. Illustration of procedure used to measure radial displacements for a geomembrane on top of compacted clay.

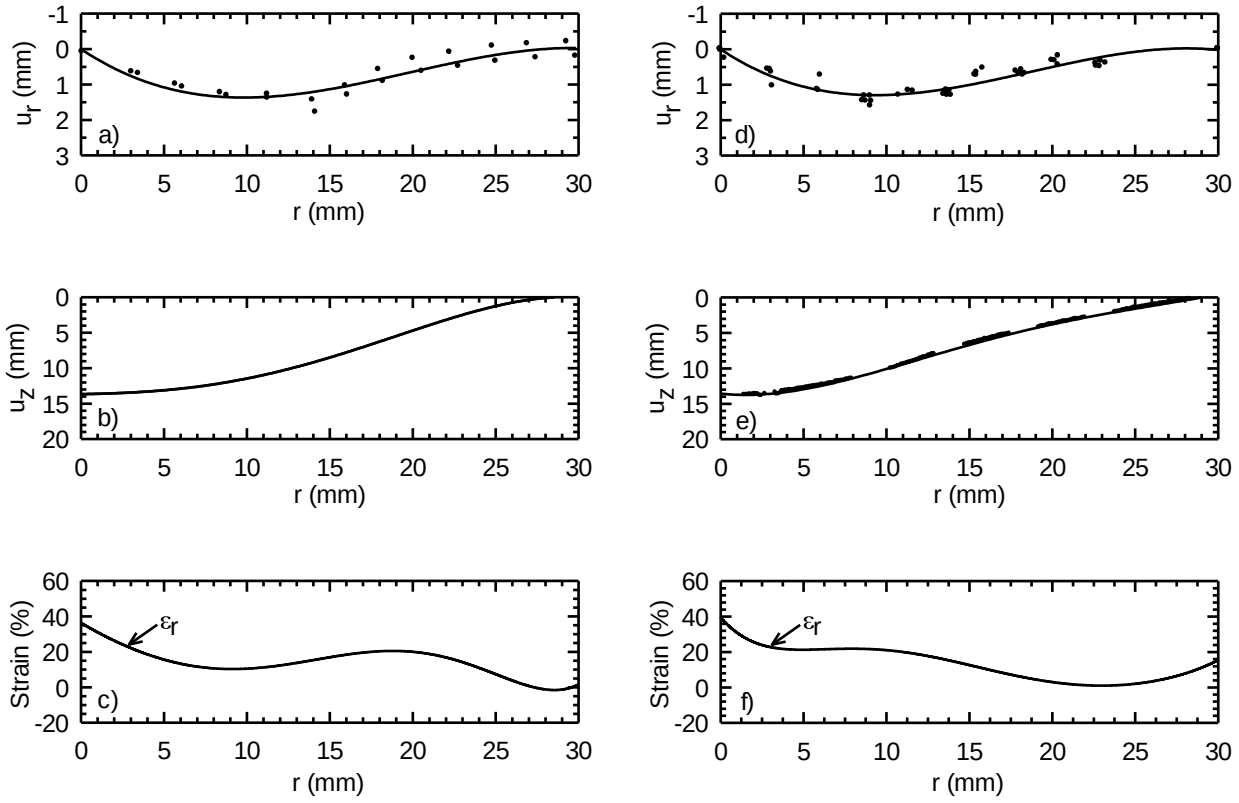

Fig. 2.17. Comparison between radial (u_r) and vertical (u_z) components of displacement and calculated strain at a prescribed displacement of 14 mm for the case with clay beneath the geomembrane: a), b), and c) and with no clay beneath the geomembrane: d), e), and f).

Chapter 3

Screening tests to help limit local geomembrane strains from gravel indentations

3.1 Introduction

Protection layers are required to prevent long-term rupture of geomembranes that line the bottom of municipal solid waste landfills. The issue examined here is limiting tensile strains in the geomembrane that develop at local indentations from overlying gravel particles when subject to the weight of the overlying waste, Fig. 3.1. These local tensions need to be limited to ensure adequate long-term performance of the geomembrane (Seeger and Müller, 2003; Rowe et al. 2004).

The magnitude of local strains in municipal solid waste landfill geomembranes may be expected to depend on: the magnitude of the vertical stress acting on the geomembrane, which will depend on the depth, type, age and water content of the waste; the particle size, particle size distribution and particle shape of the overlying material, which is commonly poorly-graded angular coarse gravel; the effectiveness of the protection layer, whether it is a nonwoven, needle-punched geotextile or a thick soil layers; the type and thickness of the geomembrane, typically 1.5-2.5 mm thick high-density polyethylene; and the compressibility of the material below the geomembrane, which normally either is a compacted clay liner or a geosynthetic clay liner. They will also depend on the service temperature of the geomembrane and the time over which the geomembrane is required to act as an effective barrier. These latter two factors impact the long-term creep of the system (i.e., geotextile protection, geomembrane, and underlying material), e.g., see Sabir and Brachman (2012).

Physical testing to assess the effectiveness of a protection layer for a given set of conditions in the laboratory may be complicated by: the scale of the equipment required to limit

boundary effects when testing coarse gravels; the time required to conduct the experiment to capture long-term creep effects; the service temperature of the landfill being 10 to 40°C hotter than ambient laboratory conditions (Koerner and Koerner, 2006; Rowe, 2012); having sufficient pieces of equipment to conduct adequate replicate experiments in a reasonable period of time; and, even how local strains are calculated from a measured deformed shape (Brachman and Eastman, 2013). There are currently three main test methods that examine the effectiveness of a geotextile protection layer. Two of the methods, LFE-2 and DIN EN 13719 (2002) are essentially identical methods that use a 300 mm diameter sample. The third method, ASTM D5514-06 (2011) inverts the profile and uses a 450 mm diameter sample. Hornsey and Wishaw (2012) recently showed that the three test methods have limitations, particularly in strain calculation, and presented a new strain measurement technique whereby the entire geomembrane surface is analyzed and has its strain calculated through the use of a handheld laser scanner.

It is suggested here that there is a role for a screening test that can reasonably simulate the physical response of a geomembrane beneath a single machined steel probe under constant vertical force under controlled and repeatable experimental conditions. Such a screening, or index test would be intended to complement, rather than replace, more elaborate large-scale physical testing of geomembrane protection with real materials. The first benefit of a screening test is that it can provide insight into how important parameters may impact local strains. Secondly, it would provide data that could be used to rule out protection layers that are unable to meet a long-term tensile strain limit, and conversely, identify those that may be able to limit strains to a target level.

The first objective of this chapter is to validate the small-scale test apparatuses used with more elaborate, larger-scale testing with real gravel by comparing geomembrane strains. The second objective is to provide insight into how key factors including the compressibility of

the underlying clay, particle size of the overlying gravel, and type of protection layer impact local geomembrane strains through screening tests. The third objective is to provide results that outline which protection layers were able to limit local geomembrane strains below a target strain which could then be used for subsequent larger scale evaluation with site specific materials.

3.2 Method

3.2.1 Test apparatus

The two test apparatuses used in this study are shown in Fig. 3.2. The dimensions and boundary conditions were selected to simulate the mean local strains induced by nominal 50 and 25 mm gravel. The apparatuses had inside diameters of 60 and 35 mm respectively which correspond to the mean centre-to-centre spacing between gravel contacts for nominal 50 and 25 mm coarse gravel overlying a geomembrane (Brachman and Gudina, 2008). The geomembrane was gripped between grooved steel flanges resulting in zero radial and vertical displacement boundary conditions around the perimeter of the geomembrane.

Brachman and Gudina (2008) found that of the five common types of contacts identified, point contacts were the most common. They found average indentation widths of 28 and 19 mm from point contacts for nominal 50 and 25 mm coarse gravels. Thus, steel probes were machined with diameters of 28 and 19 mm and narrowed to a point where it contacted the geomembrane to simulate the mean response of 50 and 25 mm gravel.

A constant vertical force was applied to the steel probe. This was achieved by hanging weights with a lever arm using a modified oedometer frame. Force was selected based on the average vertical stress acting on the geomembrane multiplied by the average contact spacing. For example, a force of 707 N was applied to the probe in the 60 mm diameter cell to reach an average applied stress of 250 kPa. Likewise, 240 N was applied in the 35 mm diameter cell to

obtain 250 kPa. The applied force corresponds to the average contact force; however, one would expect larger and smaller values with real gravel due to the inherent variability in gravel particle geometry.

The effectiveness of the test apparatuses at reproducing the mean local strains from real gravel will be examined in a subsequent section by examining full-scale local strains from real 50 and 25 mm gravel reported by Brachman and Gudina (2008).

3.2.2 Materials

Silty-clay till acquired from a landfill in Milton, Ontario was used for the compacted clay layer in all tests. The soil was first dried and then passed through the number four sieve (4.75 mm opening). Any particles that did not pass through the sieve were removed. Properties of the resulting clay are given in Table 3.1. Standard, modified, and reduced Proctor tests were performed on the clay and the results plotted in Fig. 3.3. These tests span the range of compactive effort expected in the field and define the line of optimums needed to help identify the acceptable zone of compaction to achieve a low hydraulic conductivity for field applications (Daniel and Benson, 1990; Benson et al. 1999; Rowe et al. 2004). The clay had a specific gravity of 2.72 which was used to define the zero air voids curve for the clay. Its Standard Proctor maximum dry density was 1.9 g/cm^3 and occurred at an optimum water content of 12%. The clay was placed in the apparatus at a molding water content (w_i) of either 12 or 16% and compacted to an initial dry density (ρ_{di}) of 1.8, 1.9, or 2.02 g/cm^3. The four combinations of water content and dry density tested are denoted 1-4 in Fig. 3.3 and span the acceptable zone of compaction for this particular clay.

A 1.5-mm-thick, smooth, high-density polyethylene geomembrane (GMB) was used in all but one test where a 2.5-mm-thick high-density polyethylene geomembrane was used (GMB2). Properties of the geomembranes examined are provided in Table 3.2. For each respective

thickness, all geomembrane specimens were obtained from the same roll. Unless otherwise noted in the text or figures, the results refer to the 1.5-mm-thick geomembrane.

Three nonwoven needle-punched geotextiles (GT1-GT3) were used for geomembrane protection. Index force versus displacement results from a modified version of ASTM D6241 are displayed in Fig. 3.4. Secant values of modulus from 0 to 2 and 0 to 5 mm of vertical displacement are given in Table 3.3. Dickinson and Brachman (2008) noted that as the machined steel probe deforms into the geotextile, the thickness of the geotextile is reduced and the contact area between the probe and surrounding geotextile increases thereby spreading the contact force over a larger area. This is commonly referred to as cushioning. The contact force applied to the geomembrane from the machined steel probe is even further reduced through mobilization of membrane tensions in the geotextile, depending on the slack and stiffness of the geotextile (Dickinson and Brachman, 2008). Little force was mobilized even up to 10 mm of displacement for all three geotextiles as shown in Fig. 3.4. Hence the geotextiles would likely reduce geomembrane strains by cushioning rather than by carrying membrane tension. Two screening tests simulating 50 mm nominal gravel (250 kPa, GT1; 750 kPa, GT2), used a geotextile that did not meet the recommended mass per unit area based on the design equation outlined in Koerner et al. (2010), e.g., see Fig. 3.5. This was only done to obtain a more complete data set. In both cases, the maximum geomembrane strains exceeded proposed allowable strain limits. All other screening tests were conducted with a geotextile that met the design equation proposed by Koerner et al. (2010).

3.2.3 Procedure

Once the materials were placed in the test apparatus, a test temperature of 55°C was obtained. For reference, temperatures between 30-45°C correspond to conditions presently anticipated for most municipal solid waste landfills (Rowe, 2012). It is not the intent of the

elevated temperature to simulate an actual landfill temperature but rather to use an elevated temperature of 55°C to accelerate the creep response of the geotextiles and geomembrane. Sabir and Brachman (2012) examined the effects of time and temperature on geomembrane strain and showed that for a 1.5-mm-thick high-density polyethylene geomembrane, an experiment conducted at 55°C for 100 hours is equivalent to about 1 year of testing at a normal laboratory temperature of 22°C.

To heat the test apparatus, a 12.5-mm wide, 3-mm thick heating cable was wrapped around the outside of the test apparatus and connected to a control system. The test apparatus was then placed inside a removable insulation jacket consisting of fiberglass insulation wrapped in a silicone-coated fiberglass cloth. A thermocouple was securely placed beneath the geomembrane to ensure a constant geomembrane temperature (within ±1°C) throughout the duration of the test.

After the test temperature of 55°C was reached, vertical force was applied. Force was increased in 50 kPa increments every 12 hours. Twelve hours after the final load increment was applied, the force was then held constant for an additional 100 hours.

Upon completion of each test, the hanging weights were removed and the temperature of the test apparatus was reduced to room temperature (22 ± 2°C). The geomembrane specimen was then carefully removed and inspected. The geomembrane was not punctured in any of the tests conducted.

A thin lead sheet of 0.47 mm thickness was placed between the geomembrane and underling clay layer to preserve the final deformed shape of the geomembrane indentation. The deformed shape was then measured with a line laser scanner with an accuracy of ± 0.055 mm. Geomembrane strains were calculated based on the deformed shape using thin-shell theory as developed by Tognon et al. (2000). While Brachman and Eastman (2013) used large-strain displacement theory for one case with underlying clay and showed that thin shell theory may

underestimate the maximum geomembrane strain beneath a gravel particle, they found that thin shell theory and large strain-displacement theory are in close agreement along the side-slope of a gravel indentation (the region typically where puncture occurs).

3.3 Results and discussion

3.3.1 Screening test validation

Geomembrane strains obtained from the new test apparatuses were compared with more elaborate tests using real 50 and 25 mm coarse gravel. Brachman and Gudina (2008) conducted tests using two types of granular material, nominal 50 and 25 mm poorly graded gravel, on top of a 1.5-mm-thick high-density polyethylene geomembrane with no protection layer. Their apparatus had an inside diameter of 590 mm as shown in Fig. 3.6. Tests were conducted at an applied stress of 250 kPa and a temperature of 22°C for a duration of 10 hours.

For nominal 50 mm coarse gravel, based on 88 gravel indentations from three replicate tests (i.e. all discernible indentations), Brachman and Gudina (2008) showed that the local strains followed a standard normal distribution with a mean strain of 12% and a standard deviation of 5%. Results from three replicate tests simulating nominal 50 mm gravel yielded an average strain of 13.1% with a standard deviation of 0.16% for otherwise similar conditions as shown in Table 3.4.

For nominal 25 mm coarse gravel, Brachman and Gudina (2008) examined 134 gravel indentations from three replicate tests and again found that the local strains followed a standard normal distribution with a mean strain of 6% and a standard deviation of 3%. Results from three replicate tests simulating nominal 25 mm gravel yielded an average strain of 7.8% with a standard deviation of 0.43% for otherwise similar conditions.

An unpaired t test was carried out for both gravel sizes to compare mean geomembrane strains from Brachman and Gudina (2008) and the present study and showed that the difference

was not statistically significant at a 95% confidence interval, thereby validating that the test apparatuses are able to reproduce the mean local strains induced by nominal 50 and 25 mm gravel.

Mean geomembrane strains from 25 mm gravel were roughly half that of 50 mm gravel as outlined above. This is because when using 25 mm gravel, each gravel contact applies, on average, less force to the geomembrane. While it is expected that real gravel will produce smaller and larger strains than those from the steel probes, the probes capture the mean strain from both gravel sizes and therefore are suitable for screening tests. A fundamental advantage of using these single point test apparatuses lies in the reproduceability of test results as highlighted above.

3.3.2 Evaluation of soil compressibility

Tests were conducted at four combinations of clay water content and initial dry density that lie within the acceptable compaction zone (Fig. 3.3) to investigate the effect of clay compaction on geomembrane strains. These tests simulated nominal 50 mm gravel at an applied stress of 250 kPa. For geomembrane protection, GT2 was used as the mass of this geotextile satisfied the design equation that Koerner et al. (2010) have proposed to prevent geomembrane puncture. Maximum calculated geomembrane strains from replicate tests are reported in Table 3.5. For reference, the final water content was determined by taking a final clay sample at a depth 15 to 35 mm below the deformed surface of the clay.

Comparing results from test Series 1 (ρ_{di} = 1.9 g/cm^3, w_i = 12%) and 2 (ρ_{di} = 1.9 g/cm^3, w_i = 16%), if soil compressibility were governed solely by initial void ratio, one would expect the maximum geomembrane strain for these two test Series to be the same since they have the same initial dry density. However, on average, the strain from test Series 1 is less than one half that from test Series 2. This difference in compressibility can be attributed to soil suctions. Test

Series 1 had an initial degree of saturation (S_i) of 73% and developed suctions that effectively decreased its compressibility while test Series 2 was essentially saturated and hence had no suctions. This difference in soil compressibility is reflected in the force-displacement plot shown in Fig. 3.7 and the final deformed shape of the geomembrane provided in Fig. 3.8.

Test Series 2 and 3 (ρ_{di} = 1.8 g/cm^3, w_i = 16%) were both conducted at the same clay water content of 16% but at different initial dry densities. Test Series 2 was initially saturated while test Series 3 had an initial degree of saturation of 84%. One would expect lower suctions at the higher saturation of 84% relative to test Series 1. At the end of test Series 3, the soil was saturated from consolidation thereby eliminating any suction forces. Geomembrane strains for test Series 2 and 3 were in close agreement as reflected by the force-displacement response in Fig. 3.7 and the similarity in the final deformed shape of the geomembrane for the two test Series as shown in Fig. 3.8. The difference in soil compressibility is due to initial suctions in test Series 3 and the difference in initial dry density between test Series 2 and 3.

Test Series 1 and 4 (ρ_{di} = 2.02 g/cm^3, w_i = 12%) were also conducted at the same clay water content of 12% but at different dry densities. The geomembrane strains were almost identical between test Series 1 and 4 with the slight difference in values attributed to differences in initial suctions and initial dry density.

While geomembrane strains at a clay water content of 12% compacted to an initial dry density of 2.02 g/cm^3 were slightly lower than at a dry density of 1.9 g/cm^3, a dry density of 2.02 g/cm^3 would likely be a more challenging compaction specification to consistently achieve in the field. Thus, a clay water content of 12% and an initial dry density of 1.9 g/cm^3 were selected for the compacted clay layer when performing screening tests simulating nominal 50 and 25 mm gravel.

These results show the benefit of using a compaction water content towards the lower range of water content to achieve an acceptably low hydraulic conductivity and also limit local

strains in the geomembrane. Thus, while a large range of water contents may be acceptable in terms of achieving a low hydraulic conductivity (i.e. a region approximately bounded by points 1-4 in Fig. 3.3), there would be merit in terms of local geomembrane strain to place the final lift of a compacted clay liner towards the lower range. If relied upon to limit local geomembrane strain, good inspection and quality control would be important in the field to ensure the final lift is not placed too wet.

The impact of compaction water content on local geomembrane strains also shows the importance of good knowledge and control of water content during full-scale physical testing to evaluate the effectiveness of any protection layer. For example, as evidence by comparing test Series 1 and 2, preparation at the same compactive effort but having varying initial water content, say due to operator error, can lead to large variations in strain.

3.3.3 Screening tests: target strain

The screening tests reported in the subsequent sections were conducted for a relatively short duration of 100 hours. However, the geomembrane will be required to line the bottom of a municipal solid waste landfill for potentially as long as 100 years. A long-term creep factor is therefore needed to assess whether a short-term screening test is promising or not. Seeger and Müller (2003) proposed a long-term allowable strain limit of 3% with the intent of reducing the potential for long-term brittle rupture of the geomembrane. A target time and temperature of 100 years and 35°C were selected as this temperature is presently anticipated for most municipal solid waste landfills (Rowe, 2012). Sabir and Brachman (2012) found the ratio of the 100 year strain at 35°C to the 100 hour strain at 55°C to be approximately 2. This paper proposes a short-term target strain of 1.5% by dividing the 3% long-term allowable strain limit by the creep rate of 2. Sabir and Brachman (2012) used a clay water content of 16% rather than 12%. It is therefore assumed that the creep rate is no greater for a clay water content of 12%.

3.3.4 Screening tests: 50 mm gravel

Vertical displacements of the steel probe after each 12 hour load increment are plotted in Fig. 3.9a for the geotextiles when simulating nominal 50 mm gravel at an applied pressure of 250 kPa. Final deformed shapes of the geomembrane are shown in Fig. 3.9b. Protection from GT3 produced a smaller displacement than GT1 or GT2. This is because GT3 had the greatest mass per unit area (and hence thickness) and hence provided the most cushioning. Maximum geomembrane strains are plotted in Fig. 3.10. The long-term strain limit of 3% proposed by Seeger and Müller (2003) and the strain target of 1.5% are represented by horizontal dotted lines. At an applied stress of 250 kPa, the maximum strain of 10% with GT1 was already well above proposed allowable strain limits and was therefore not tested at higher stresses. Peak strains with GT2 also exceeded proposed allowable strain limits. Protection from GT3 met the 3% strain limit at 250 kPa, however, since this screening test was conducted for only 100 hours, it would be expected to exceed 3% after more creep.

These screening tests revealed that none of the tested geotextiles met the target strain of 1.5%. If 50 mm gravel is selected for design, a more effective protection layer such as 150 mm of sand is recommended as Brachman and Gudina (2008), and Dickinson and Brachman (2008) found maximum strains to be less than 0.5% at an applied stress of 250 kPa.

3.3.5 Screening tests: 25 mm gravel

Vertical displacements of the steel probe after each 12 hour load increment are plotted in Fig. 3.11a for the geotextiles when simulating nominal 25 mm gravel at an applied pressure of 250 kPa with final deformed geomembrane shapes provided in Fig. 3.11b. Peak geomembrane strains are plotted in Fig. 3.12. With GT1 protection, at stresses greater than 150 kPa, the maximum geomembrane strain may be expected to exceed the 3% strain limit. Even at an applied stress of 100 kPa, GT1 was unable to limit the maximum geomembrane strain below the

target strain of 1.5%. The peak geomembrane strain with GT2 was 3% at 350 kPa while the maximum geomembrane strain was below the strain target at an applied stress of 250 kPa. Protection from GT3 resulted in a peak geomembrane strain that was below 3% even at an applied stress of 750 kPa. Furthermore, this protection layer successfully limited geomembrane strains below 1.5% at 500 kPa. At an applied stress of 750 kPa, placing geotextiles in the form of a layered geotextile protection layer without any adhesive (GT2+GT3) reduced the peak geomembrane strain to 0.8%. In addition, a thicker geomembrane (GMB2) with GT3 protection met the 1.5% target strain.

3.4 Conclusions

The test apparatuses used were validated by comparing geomembrane strains with more elaborate, larger-scale testing with real gravel. Small-scale screening tests were conducted to provide insight into how key factors including the compressibility of the underlying clay, particle size of the overlying gravel, and type of protection layer influence local geomembrane strains. Results were provided which identify protection layers that successfully limited strains below a target strain of 1.5%. Given the idealizations required to produce the repeatable and controlled experimental conditions, tests with the new apparatuses are meant to complement, rather than replace, more elaborate large-scale geomembrane testing with real materials (e.g., Brachman and Gudina 2008; Dickinson and Brachman 2008). For the particular conditions examined, the main findings are:

a) Screening test validation: Results were compared between the test apparatuses used and more elaborate, larger-scale testing with real gravel. The test apparatuses were shown to reproduce the mean response for 50 and 25 mm gravel in short term tests.
b) Evaluation of soil compressibility: Compaction water contents towards the lower range of water content to achieve an acceptably low hydraulic conductivity were found to be more

successful in limiting local strains in the geomembrane. While a large range of water contents may be acceptable in terms of achieving a low hydraulic conductivity, there would be merit in terms of local geomembrane strains to place the final lift of a compacted clay liner towards the lower range. The impact of compaction water content on local geomembrane strains also shows the importance of good knowledge and control of water content during full-scale physical testing to evaluate the effectiveness of any protection layer.

c) Screening tests simulating nominal 50 mm gravel: Screening tests with 50 mm gravel revealed that none of the tested geotextiles met the proposed strain target of 1.5%. If 50 mm gravel is selected for design, a more effective protection layer such as 150 mm of sand is recommended.

d) Screening tests simulating nominal 25 mm gravel: Screening tests with 25 mm gravel revealed that the maximum strain with GT2 was below the 1.5% strain target at an applied stress of 250 kPa while GT3 limited the peak geomembrane strain below the strain target up to 500 kPa. At an applied stress of 750 kPa, adding geotextiles in the form of a layered geotextile protection layer (GT2+GT3) reduced the peak geomembrane strain to 0.8%. In addition, a thicker geomembrane (GMB2) with GT3 protection met the strain target.

3.5 References

ASTM D5514-06, 2011. Large scale hydrostatic puncture testing of geosynthetics.

ASTM D6241-04, 2009. Standard test method for the static puncture strength of geotextiles and geotextile-related products using a 50-mm probe.

Benson, C.H., Daniel, D.E., Boutwell, G.P., 1999. Field performance of compacted clay liners. Journal of Geotechnical and Geoenvironmental Engineering 125 (5), 390-403.

Brachman, R.W.I., Eastman, M.K., 2013. Calculating local geomembrane indentation strains from measured radial and vertical displacements. Geotextiles and Geomembranes 40, 58-68.

Brachman, R.W.I., Gudina, S., 2008. Gravel contacts and geomembrane strains for a GM/CCL composite liner. Geotextiles and Geomembranes 26 (6), 448-459.

Brachman, R.W.I., Sabir, A., 2013. Long-term assessment of a layered-geotextile protection layer for geomembranes. Journal of Geotechnical and Geoenvironmental Engineering 139 (5), 752-764.

Daniel, D., Benson, C., 1990. Water content-density criteria for compacted soil liners. Journal of Geotechnical Engineering, ASCE, 116 (12), 1811-1830.

Dickinson, S., Brachman, R.W.I., 2008. Assessment of alternative protection layers for a geomembrane / geosynthetic clay liner (GM/GCL) composite liner. Canadian Geotechnical Journal 45 (11), 1594-1610.

DIN EN 13719, 2002. Geotextiles and geotextile-related products – determination of the long term protection efficiency of geotextiles in contact with geosynthetic barriers.

Gudina, S., Brachman, R.W.I., 2006. Physical response of geomembrane wrinkles overlying compacted clay. Journal of Geotechnical and Geoenvironmental Engineering 132 (10), 1346-1353.

Hornsey, W.P., Wishaw, D.M., 2012. Development of a methodology for the evaluation of geomembrane strain and relative performance of cushion geotextiles. Geotextiles and Geomembranes 35, 87-99.

Koerner, G.R., Koerner, R.M., 2006. Long-term temperature monitoring of geomembranes at dry and wet landfills. Geotextiles and Geomembranes 24 (1), 72-77.

Koerner, R.M., Hsuan, Y.G., Koerner, G.R., Gryger, D., 2010. Ten year creep puncture study of HDPE geomembranes protected by needle-punched nonwoven geotextiles. Geotextiles and Geomembranes 28 (6), 503-513.

LFE-2 Cylinder testing geomembranes and their protective materials. A methodology for testing protector geotextiles for their performance in specific site conditions.

Narejo, D., Koerner, R.M., Wilson-Fahmy, R.F., 1996. Puncture protection of geomembranes Part II: Experimental. Geosynthetics International 3 (5), 629-653.

Rowe, R.K., 2012. Short and long-term leakage through composite liners, The 7th Arthur Casagrande Lecture, Canadian Geotechnical Journal 49 (2), 141-169.

Rowe, R.K, Islam, M.Z., Hsuan, Y.G., 2010. Effect of thickness on the ageing of HDPE geomembranes. Journal of Geotechnical and Geoenvironmental Engineering 136 (2), 299-309.

Rowe, R.K., Quigley, R.M., Brachman, R.W.I., and Booker, J.R., 2004. Barrier Systems for Waste Disposal Facilities. 2nd Ed., E & FN Spon, London, 587 pp.

Sabir, A., Brachman, R.W.I., 2012. Time and temperature effects on geomembrane strain from a gravel particle subject to sustained vertical force. Canadian Geotechnical Journal, 49 (3), 249-263.

Seeger, S., Müller, W., 2003. Theoretical approach to designing protection: selecting a geomembrane strain criterion. Geosynthetics: Protecting the Environment. Dixon, N., Smith, D.M., Greenwood, J.H., Jones, D.R.V. (Eds.), Thomas Telford, London, 137-152.

Tognon, A.R., Rowe, R.K., Moore, I.D., 2000. Geomembrane strain observed in large-scale testing of protection layers. Journal of Geotechnical and Geoenvironmental Engineering 126 (12), 1194-1208.

Table 3.1: Properties of the clay examined.

Property	Value
Plastic limit (%)	16[a]
Liquid limit (%)	26[a]
Std Proctor optimum water content (%)	12
Std Proctor maximum dry density (g/cm^3)	1.9
Specific gravity (-)	2.72

[a]From Brachman and Sabir (2013)

Table 3.2: Properties of the geomembranes examined.

Property	Direction	GMB[a]		GMB2[b]	
		Mean	Std dev.	Mean	Std dev.
Yield strength (kN/m)	Machine	27	1.0	45.8	1.7
Break strength (kN/m)		46	5.0	62.3	10.2
Yield strain (%)		24	2.0	20.3	0.51
Break strain (%)		830	80	767	58
Yield strength (kN/m)	Cross-machine	29	1.0	46.9	0.56
Break strength (kN/m)		44	6.0	38.5	8.4
Yield strain (%)		19	1.0	19.4	0.75
Break strain (%)		830	95	634	143
Crystallinity (%)	-	44	4.0	46.6	1.7

[a]From Brachman and Sabir (2013)
[b]From Rowe et al. (2010)

Table 3.3: Properties of the nonwoven needle-punched geotextiles examined.

Designation	Mass (g/m^2)	Thickness (mm)	Secant modulus (N/mm)	
			0-2 mm	0-5 mm
GT1	560	4.1	1.3	1.4
GT2	1500	6.8	2.4	3.4
GT3	2440	11	5.5	7.4

Table 3.4: Comparison of average strains from real 25 and 50 mm coarse gravel with the modified test apparatus and steel probes.

Gravel size	Real gravel (%)[a]		Steel probe (%)				
	Mean	Std dev.	a	b	c	Mean	Std dev.
50 mm	12	5.0	13.1	13.3	12.9	13.1	0.16
25 mm	6.0	3.0	8.3	7.8	7.3	7.8	0.43

[a]From Brachman and Gudina (2008)
Note: a, b, and c denote replicate tests.

Table 3.5: Summary of tests examining soil compressibility.

Gravel size	Test	w_i (%)	ρ_{di} (g/cm^3)	S_i (%)	w_f (%)	ρ_{df} (g/cm^3)	S_f (%)	Strain (%)				
								a	b	c	Mean	Std dev.
50 mm	1	12	1.9	73	10.2	-	-	5.1	3.9	4.0	4.3	0.5
	2	16	1.9	100	13.1	2.01	100	9.8	9.7	8.4	9.3	0.6
	3	16	1.8	84	13.5	1.99	100	10.3	10.0	10.4	10.2	0.2
	4	12	2.02	94	10.6	2.18	100	4.3	4.0	-	4.2	0.2

Note: a, b, and c denote replicate tests.

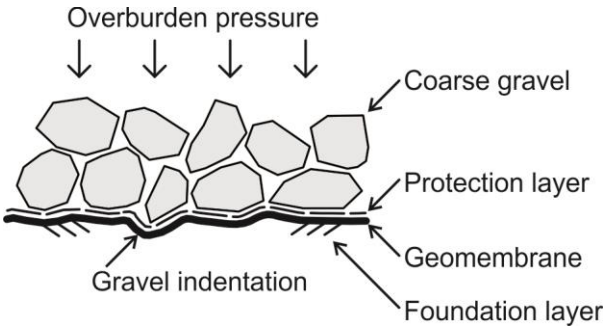

Fig. 3.1. Geomembrane indentation induced by overlying coarse gravel.

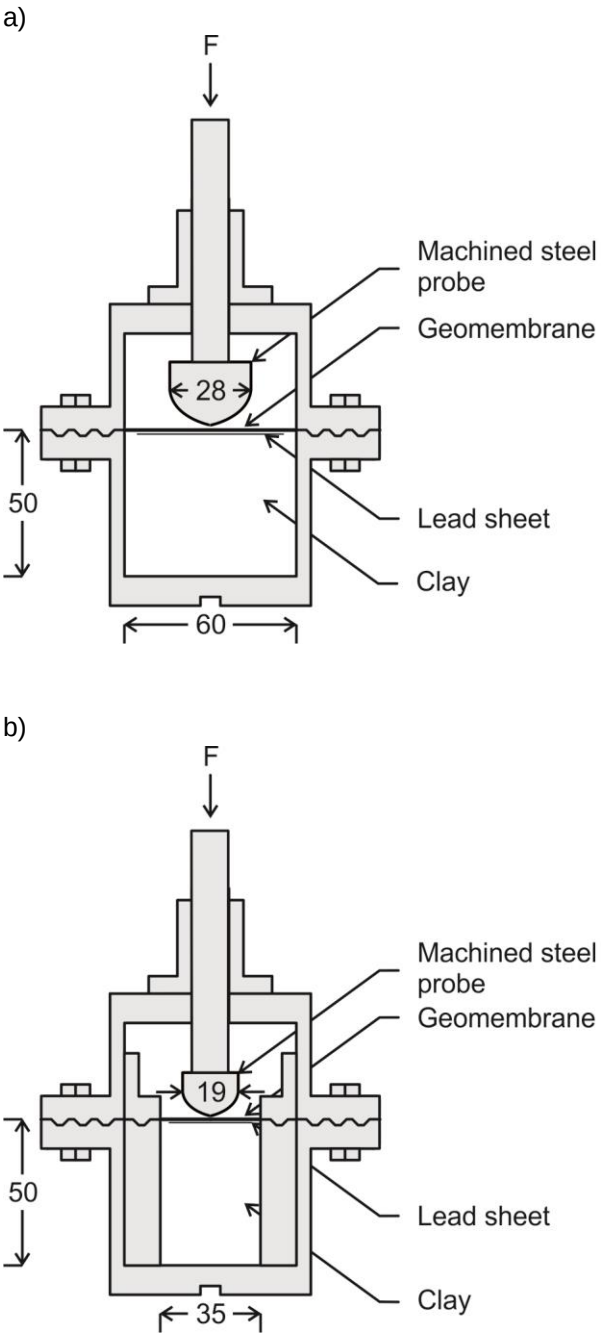

Fig. 3.2. Cross section of test apparatus: a) 50 mm nominal gravel, and b) 25 mm nominal gravel. Dimensions in mm.

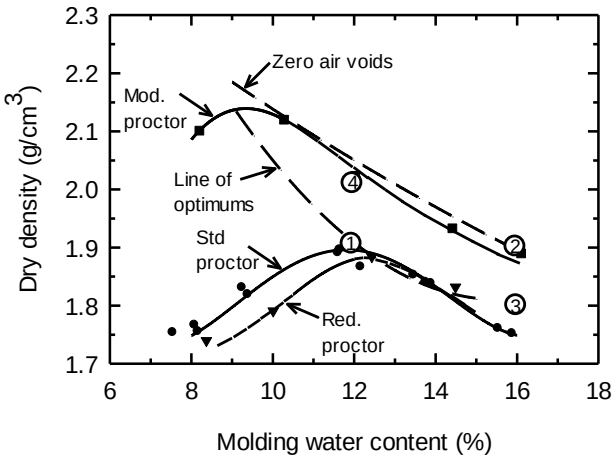

Fig. 3.3. Standard, modified, and reduced Proctor tests with line of optimums and zero air voids curve. Configurations of water content and dry density denoted 1-4.

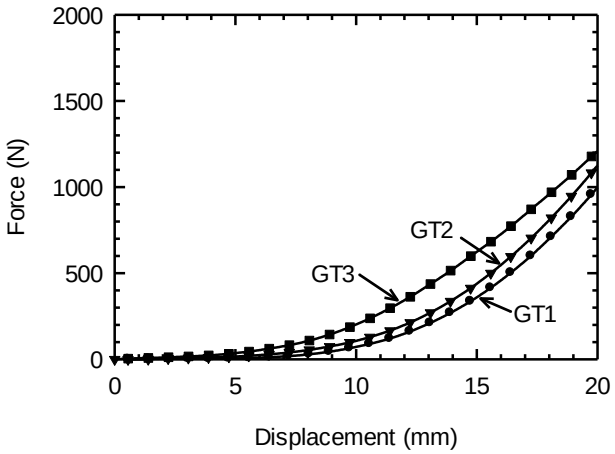

Fig. 3.4. Index force-deflection results from modified ASTM D6241 test on four nonwoven geotextiles used as protection layers with GP50.

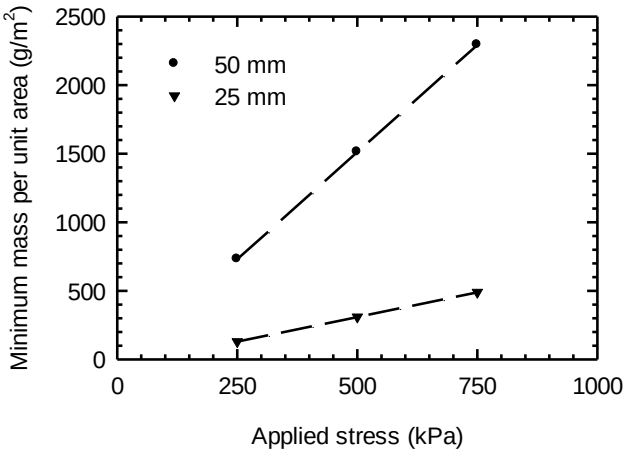

Fig. 3.5. Minimum mass per unit area based on the design equation from Koerner et al. (2010).

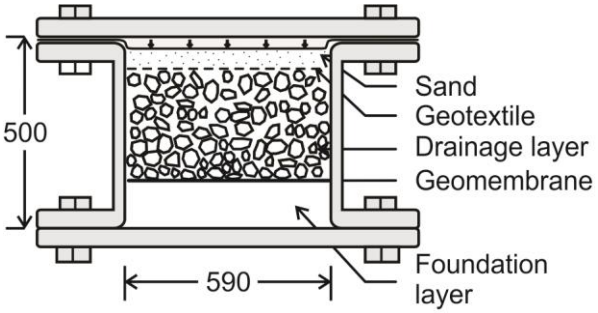

Fig. 3.6. Cross-section through apparatus used in Brachman and Gudina (2008). Dimensions in mm.

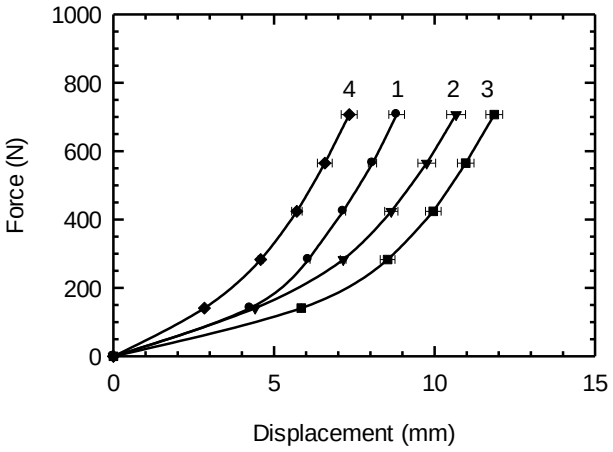

Fig. 3.7. Mean force-displacement response after each 12-h load increment for test Series 1 (ρ_{di} = 1.9 g/cm^3, w_i = 12%); 2 (ρ_{di} = 1.9 g/cm^3, w_i = 16%); 3 (ρ_{di} = 1.8 g/cm^3, w_i = 16%); and 4 (ρ_{di} = 2.02 g/cm^3, w_i = 12%).

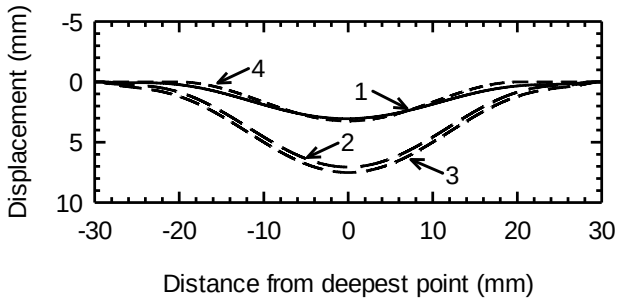

Fig. 3.8. Final deformed shape of the geomembrane for test Series 1 (ρ_{di} = 1.9 g/cm^3, w_i = 12%); 2 (ρ_{di} = 1.9 g/cm^3, w_i = 16%); 3 (ρ_{di} = 1.8 g/cm^3, w_i = 16%); and 4 (ρ_{di} = 2.02 g/cm^3, w_i = 12%).

a)

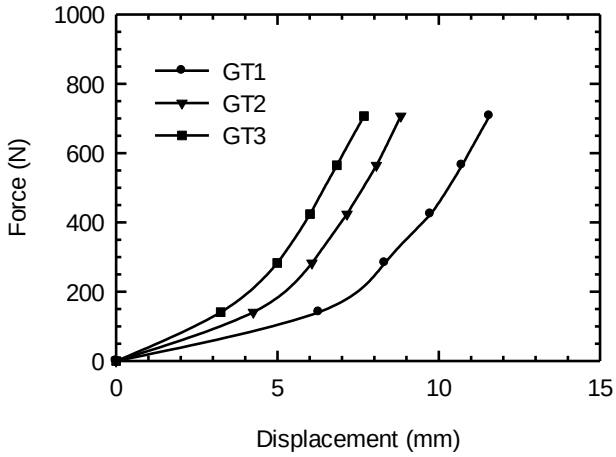

b)

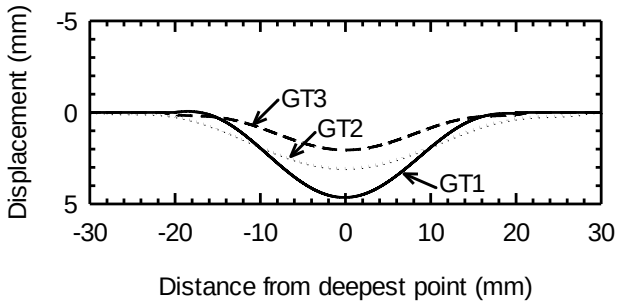

Fig. 3.9. a) Vertical displacement of the steel probe after each 12 hour load increment, and b) final deformed shape of the geomembrane when simulating nominal 50 mm gravel at an applied stress of 250 kPa.

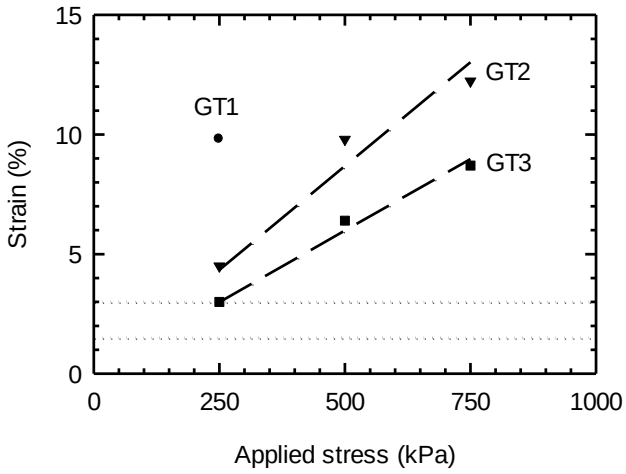

Fig. 3.10. Maximum geomembrane strains when simulating nominal 50 mm gravel with geotextile protection. The long-term strain limit of 3% proposed by Seeger and Müller (2003) and the strain target of 1.5% are represented by horizontal dotted lines.

a)

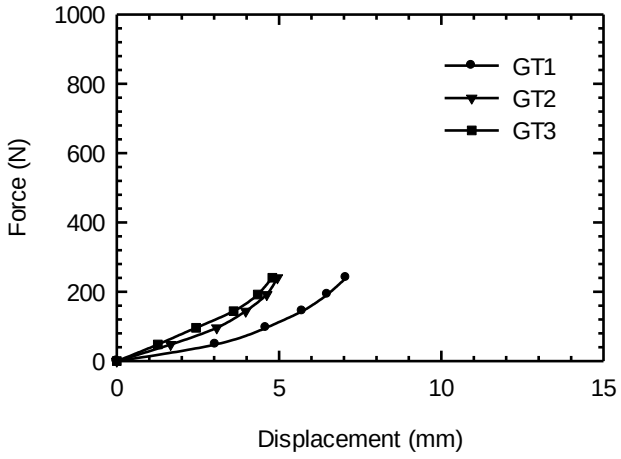

b)

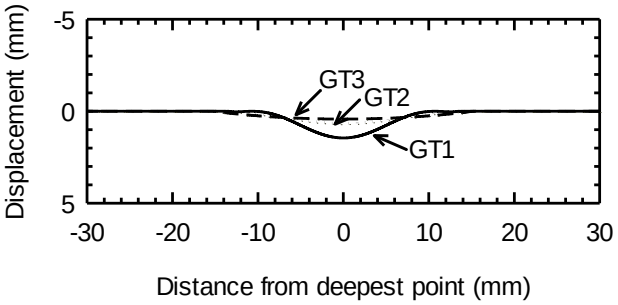

Fig. 3.11. a) Vertical displacement of the steel probe after each 12 hour load increment, and b) final deformed shape of the geomembrane when simulating nominal 25 mm gravel at an applied stress of 250 kPa.

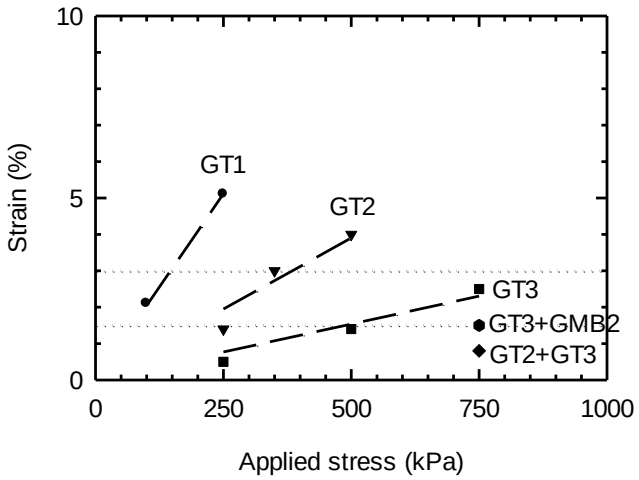

Fig. 3.12. Maximum geomembrane strains when simulating nominal 25 mm gravel with geotextile protection. The long-term strain limit of 3% proposed by Seeger and Müller (2003) and the strain target of 1.5% are represented by horizontal dotted lines.

Chapter 4

Conclusions and recommendations

4.1 Conclusions

This thesis focused on methods to calculate and minimize tensile strains in landfill geomembranes from local gravel indentations. In focusing on how strains are obtained from local indentations in the geomembrane in Chapter 2, radial displacements were found to be small relative to vertical displacements, but not negligible when calculating local geomembrane strains. They were shown to provide the dominant contribution to the maximum strain beneath the centre of the round and cone shaped probes, as it is the rate of change of radial displacement away from the indentation centre (i.e. $\partial u_r/\partial r$) rather than its magnitude alone that governs the resulting strain. The shape of the probe deforming the geomembrane was shown to impact both the magnitude and distribution of radial displacements, and hence the resulting maximum strain. For both the round and cone probes, the maximum strain in the geomembrane was located directly beneath the centre of the probe, while the maximum strain with the flat probe was located near the edge of the probe. Both the thin shell and arc elongation methods produced incorrect distributions of strain and also provided magnitudes that significantly underestimated the maximum geomembrane strain. While it is well understood that the arc elongation method assumes a uniform distribution of strain and hence underestimates the maximum strain beneath a gravel contact, it was shown that the thin shell method assumption of only vertical geomembrane displacements results in strain calculations that may underestimate the maximum strain. While large-strain displacement theory was used for one case with underlying clay, this strain calculation method is not practical for larger scale testing with a foundation layer as it would be difficult to track radial displacements. The goal here was to quantify the uncertainty in using a common strain calculation method (thin shell theory).

In Chapter 3, small-scale screening tests were conducted to provide insight into how key factors influence local geomembrane strains. Results were compared between the test apparatuses used and more elaborate, larger-scale testing with real gravel. The test apparatuses were shown to reproduce the mean response for 50 and 25 mm gravel. Compaction water contents towards the lower range of water content to achieve an acceptably low hydraulic conductivity of field compacted clay were found to be more successful in limiting local strains in the geomembrane. While a large range of water contents may be acceptable in terms of achieving a low hydraulic conductivity, there would be merit in terms of local geomembrane strains to place the final lift of a compacted clay liner towards the lower range. The impact of compaction water content on local geomembrane strains also shows the importance of good knowledge and control of water content during full-scale physical testing to evaluate the effectiveness of any protection layer. Screening tests simulating nominal 50 mm gravel revealed that none of the tested geotextiles met the proposed strain target of 1.5%. If 50 mm gravel is selected for design, a more effective protection layer such as 150 mm of sand is recommended. Screening tests simulating nominal 25 mm gravel revealed that the maximum strain with GT2 was below the 1.5% strain target at an applied stress of 250 kPa while GT3 limited the peak geomembrane strain below the strain target up to 500 kPa. At an applied stress of 750 kPa, adding geotextiles in the form of a layered geotextile protection layer (GT2+GT3) reduced the peak geomembrane strain to 0.8%. In addition, a thicker geomembrane (GMB2) with GT3 protection met the 1.5% strain target.

4.2 Recommendations for future work

The results reported in this thesis examined the response of a geomembrane when tested under controlled conditions in a small-scale apparatus for short durations. It is recommended that the screening tests provided in Chapter 3 be conducted for longer durations

to gain a better understanding of the long-term creep factor for the particular conditions used. Additional screening tests should also be conducted with thicker nonwoven needle-punched geotextiles for the case of simulating nominal 50 mm gravel to try and meet the strain target of 1.5% at an applied stress of 250 kPa. Furthermore, the effectiveness of using a geosynthetic clay liner beneath the geomembrane should be examined for both gravel sizes.

Appendix A

Final deformed shape of the geomembrane

The following Appendix presents the final deformed shape of the geomembrane from tests simulating both nominal 50 and 25 mm gravel reported in Chapter 3.

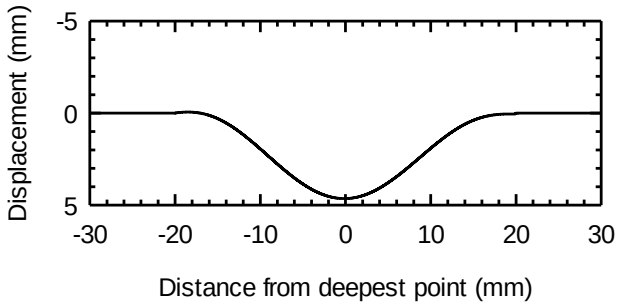

Fig. A.1. Final deformed shape of the geomembrane when simulating nominal 50 mm gravel using GT1 protection at an applied stress of 250 kPa.

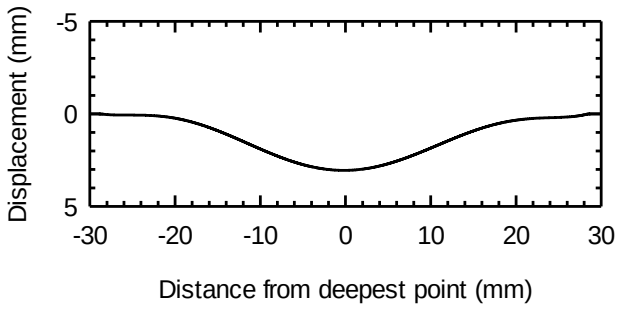

Fig. A.2. Final deformed shape of the geomembrane when simulating nominal 50 mm gravel using GT2 protection at an applied stress of 250 kPa.

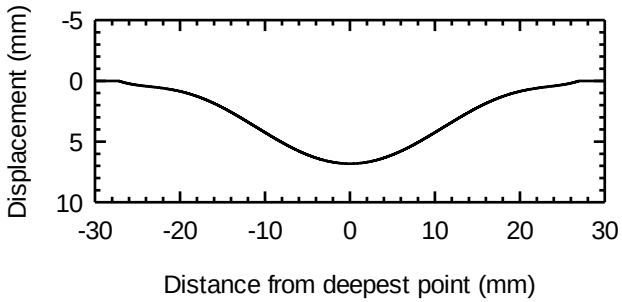

Fig. A.3. Final deformed shape of the geomembrane when simulating nominal 50 mm gravel using GT2 protection at an applied stress of 500 kPa.

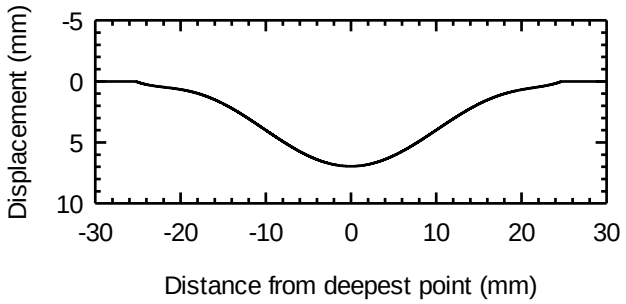

Fig. A.4. Final deformed shape of the geomembrane when simulating nominal 50 mm gravel using GT2 protection at an applied stress of 750 kPa.

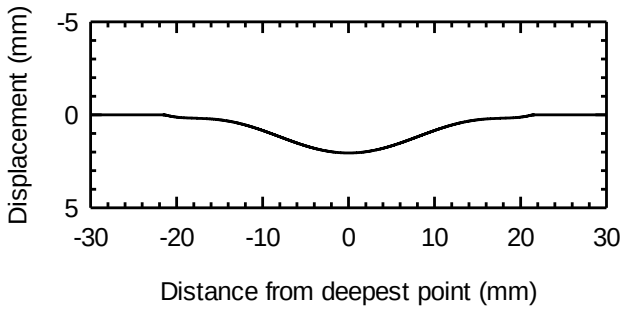

Fig. A.5. Final deformed shape of the geomembrane when simulating nominal 50 mm gravel using GT3 protection at an applied stress of 250 kPa.

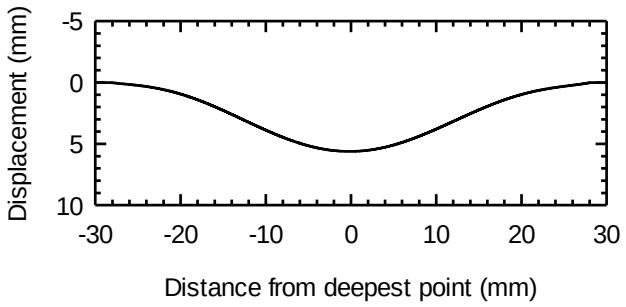

Fig. A.6. Final deformed shape of the geomembrane when simulating nominal 50 mm gravel using GT3 protection at an applied stress of 500 kPa.

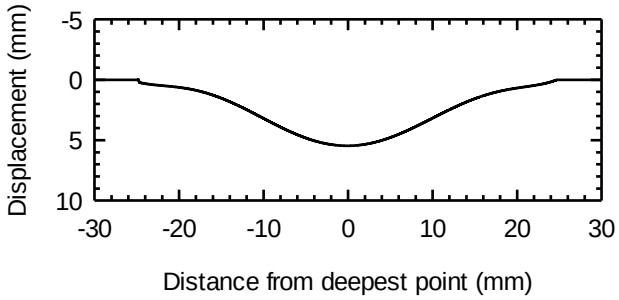

Fig. A.7. Final deformed shape of the geomembrane when simulating nominal 50 mm gravel using GT3 protection at an applied stress of 750 kPa.

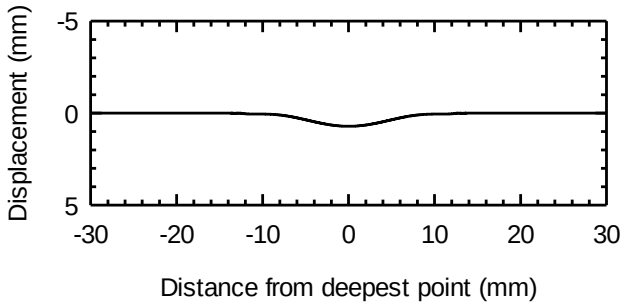

Fig. A.8. Final deformed shape of the geomembrane when simulating nominal 25 mm gravel using GT1 protection at an applied stress of 100 kPa.

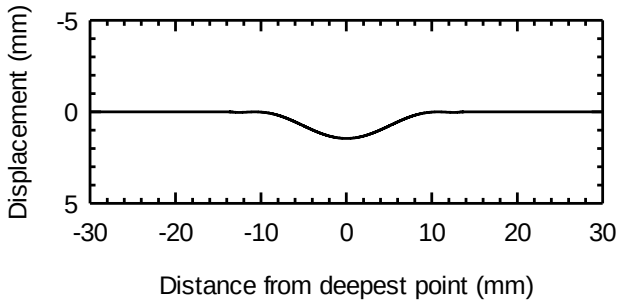

Fig. A.9. Final deformed shape of the geomembrane when simulating nominal 25 mm gravel using GT1 protection at an applied stress of 250 kPa.

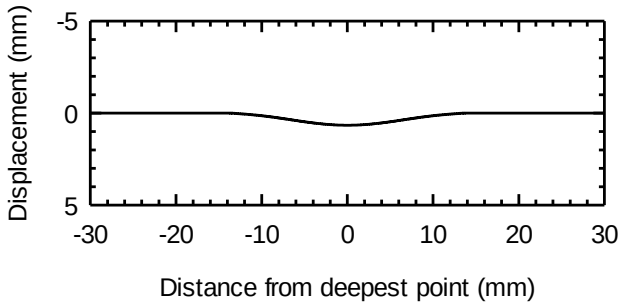

Fig. A.10. Final deformed shape of the geomembrane when simulating nominal 25 mm gravel using GT2 protection at an applied stress of 250 kPa.

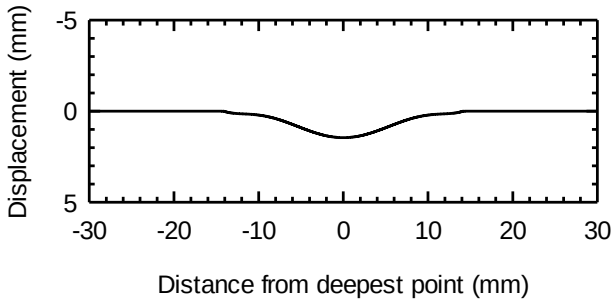

Fig. A.11. Final deformed shape of the geomembrane when simulating nominal 25 mm gravel using GT2 protection at an applied stress of 350 kPa.

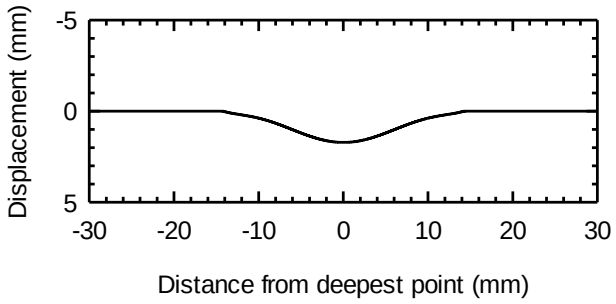

Fig. A.12. Final deformed shape of the geomembrane when simulating nominal 25 mm gravel using GT2 protection at an applied stress of 500 kPa.

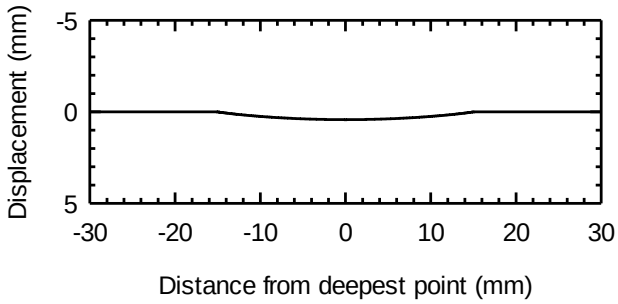

Fig. A.13. Final deformed shape of the geomembrane when simulating nominal 25 mm gravel using GT3 protection at an applied stress of 250 kPa.

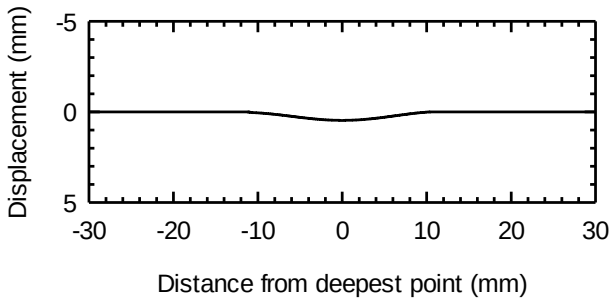

Fig. A.14. Final deformed shape of the geomembrane when simulating nominal 25 mm gravel using GT3 protection at an applied stress of 500 kPa.

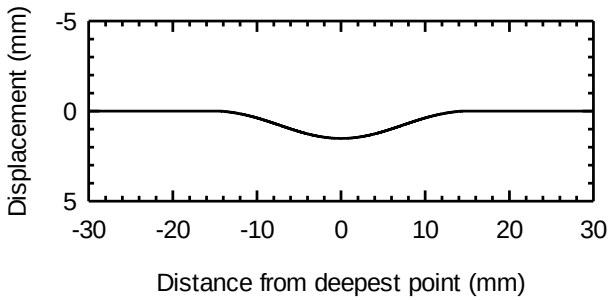

Fig. A.15. Final deformed shape of the geomembrane when simulating nominal 25 mm gravel using GT3 protection at an applied stress of 750 kPa.

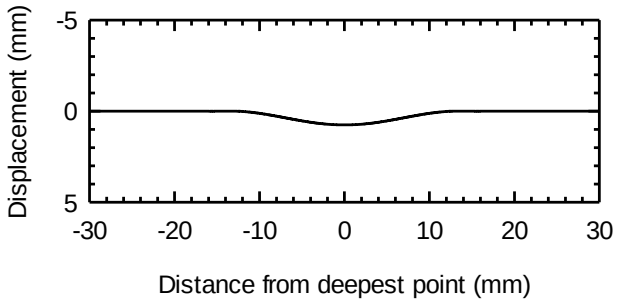

Fig. A.16. Final deformed shape of the geomembrane when simulating nominal 25 mm gravel using GMB2 and GT3 protection at an applied stress of 750 kPa.

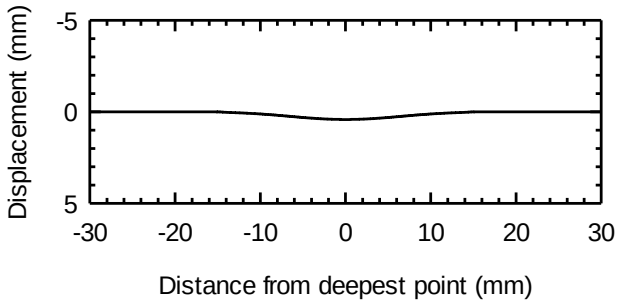

Fig. A.17. Final deformed shape of the geomembrane when simulating nominal 25 mm gravel using GT2+GT3 protection at an applied stress of 750 kPa.

Appendix B

Standard, modified, and reduced Proctor tests

Standard, modified, and reduced Proctor tests as per ASTM D698 and ASTM D1557 where conducted for the clay tested in Chapter 3. Results of dry density (ρ_d) and water content (w) are given in this Appendix.

Table B.1: Standard Proctor test results.

w	ρ_d
%	g/cm^3
7.5	1.75
9.3	1.83
12.2	1.87
13.5	1.85
8.2	1.76
9.4	1.82
11.6	1.90
13.9	1.84
15.5	1.76
8.1	1.77
11.6	1.89
13.8	1.84
15.9	1.75

Table B.2: Modified Proctor test results.

w	ρ_d
%	g/cm^3
8.2	2.10
10.3	2.12
12.0	2.02
14.4	1.93
16.1	1.89

Table B.3: Reduced Proctor test results.

w	ρ_d
%	g/cm^3
8.4	1.74
10.0	1.79
12.4	1.88
14.5	1.83

Appendix C

Specific gravity test

A specific gravity (G_s) test as per ASTM D854 was conducted for the clay tested in Chapter 3. Results are given in this Appendix.

Table C.1: Specific gravity test results.

	Flask 1	Flask 2	Flask 3	Mean
G_s	2.72	2.72	2.73	2.72